Distinguishing black-hole spin-orbit resonances by their gravitational wave signatures. II. Full parameter estimation

Daniele Trifirò, Richard O'Shaughnessy, Davide Gerosa, Emanuele Berti, Michael Kesden, Tyson Littenberg, and Ulrich Sperhake

Distinguishing black-hole spin-orbit resonances by their gravitational wave signatures. II: Full parameter estimation

Daniele Trifirò,[1, 2, *] Richard O'Shaughnessy,[3, †] Davide Gerosa,[4, ‡] Emanuele
Berti,[2, 5, §] Michael Kesden,[6, ¶] Tyson Littenberg,[7, **] and Ulrich Sperhake[4, 2, 8, ††]

[1]*Dipartimento di Fisica E. Fermi, Università di Pisa, Pisa 56127, Italy*
[2]*Department of Physics and Astronomy, The University of Mississippi, University, MS 38677, USA*
[3]*Center for Computational Relativity and Gravitation,*
Rochester Institute of Technology, Rochester, NY 14623, USA
[4]*Department of Applied Mathematics and Theoretical Physics, Centre for Mathematical Sciences,*
University of Cambridge, Wilberforce Road, Cambridge CB3 0WA, UK
[5]*CENTRA, Departamento de Física, Instituto Superior Técnico,*
Universidade de Lisboa, Avenida Rovisco Pais 1, 1049 Lisboa, Portugal
[6]*Department of Physics, The University of Texas at Dallas, Richardson, TX 75080, USA*
[7]*Center for Interdisciplinary Exploration and Research in Astrophysics (CIERA) & Department of Physics and Astronomy,*
Northwestern University, 2145 Sheridan Road, Evanston, IL 60208
[8]*California Institute of Technology, Pasadena, CA 91125, USA*

Gravitational waves from coalescing binary black holes encode the evolution of their spins prior to merger. In the post-Newtonian regime and on the precession timescale, this evolution has one of three morphologies, with the spins either librating around one of two fixed points ("resonances") or circulating freely. In this work we perform full parameter estimation on resonant binaries with fixed masses and spin magnitudes, changing three parameters: a conserved "projected effective spin" ξ and resonant family $\Delta\Phi = 0, \pi$ (which uniquely label the source); the inclination θ_{JN} of the binary's total angular momentum with respect to the line of sight (which determines the strength of precessional effects in the waveform); and the signal amplitude. We demonstrate that resonances can be distinguished for a wide range of binaries, except for highly symmetric configurations where precessional effects are suppressed. Motivated by new insight into double-spin evolution, we introduce new variables to characterize precessing black hole binaries which naturally reflects the timescale separation of the system and therefore better encode the dynamical information carried by gravitational waves.

I. INTRODUCTION

Gravitational waves (GWs) from binary black holes (BBHs) are expected to be an important source [1–4] for future networks of GW detectors such as Advanced LIGO/Virgo [5, 6], LIGO-India [7], KAGRA [8, 9], and the Einstein Telescope [10]. Once formed, BBHs emit GWs that extract energy and angular momentum from the orbit, decreasing the binary separation and increasing the orbital frequency (and thus the GW frequency). Most binaries are expected to circularize by the time they enter the sensitivity band of ground-based detectors [11, 12] (see e.g. [13–17] and references therein for recent work on eccentric binary waveforms, rates and detection strategies). Circular BBH inspirals are characterized by the masses (m_1, m_2) and spins $(\mathbf{S}_1, \mathbf{S}_2)$ of each black hole. The spin and orbital angular momenta

precess on timescales shorter than the radiation-reaction timescale [18–20]. Their general evolution can be understood relative to the two one-parameter families of fixed points ("post-Newtonian resonances") of the orbit-averaged spin precession equations [21]. At resonance, the spins and orbital angular momentum $\mathbf{L}$ remain coplanar. If $\Delta\Phi$ denotes the angle between the projection of the spins in the orbital plane orthogonal to $\mathbf{L}$, the spins can either lie on the same side of $\mathbf{L}$ (the $\Delta\Phi = 0$ resonance) or on opposite sides of $\mathbf{L}$ (the $\Delta\Phi = \pi$ resonance). In general, the conservative evolution of the spins of any BBH can be understood as either a trapped phase-space orbit around one of the two fixed points ($\Delta\Phi = 0$ and $\Delta\Phi = \pi$) or as an orbit where $\Delta\Phi$ circulates freely. Therefore the phase space can be split into three classes, or "morphologies" [22, 23].

The morphology of BBHs in the Advanced LIGO/Virgo band is determined by the spin configuration when the compact binary is first formed, long prior to its detection via GWs [24]. This relationship may enable GW measurements to constrain the efficiency of tidal interactions in binary star evolution and may indicate whether a mechanism such as mass transfer, stellar winds, or supernovae can induce mass-ratio reversal (so that the heavier black hole is produced by the initially lighter stellar progenitor). More broadly,

* daniele.trifiro@ligo.org
† rossma@rit.edu
‡ d.gerosa@damtp.cam.ac.uk
§ eberti@olemiss.edu
¶ kesden@utdallas.edu
** tyson.littenberg@northwestern.edu
†† u.sperhake@damtp.cam.ac.uk

spin measurements of BBHs have long been expected to be a critical element in distinguishing the underlying astrophysical model for compact binary formation, complementing other measurements: see e.g. [25–28].

Gravitational radiation encodes the dynamics and properties of the inspiralling binary. Precessing binaries produce a rich, highly modulated signal [18–20, 29–34], enabling constraints on compact binary parameters, such as masses and the misaligned spins [35–41]. This information can be recovered from detector measurements by systematically comparing all possible candidate signals with the data and constructing a Bayesian posterior probability distribution for all binary parameters [41–48]. Out of all precessing BBH configurations possible a priori, the two librating morphologies are relatively common for comparable-mass binaries in the close orbits to which LIGO is sensitive, but relatively rare for binaries drawn from a uniform mass distribution [23].

That said, because the relative spin dynamics do not directly source the dominant GW signal, it is important to investigate the extent to which the relative orientation of precessing spins can be constrained in general, and the degree to which measurements distinguish morphologies in particular. Vitale et al. [40] recently studied this problem for a small sample of precessing binaries, claiming that the relative angle $\Delta\Phi$ between the projection of the two spins into the orbital plane cannot be measured.

Previously, Gerosa et al. [49] examined the GW signal from the two resonant families and evaluated the overlap between the waveforms with all parameters fixed, to demonstrate that the two families produce qualitatively and quantitatively distinct GW signatures. Gupta and Gopakumar [50] used overlaps to imply resonant and non-resonant binaries were distinguishable. In this work we apply the state-of-the-art LALINFERENCE parameter estimation code [48] to the expected detector response due to resonant post-Newtonian binaries in the nearby Universe. Using the posterior distribution of compact binary parameters, we assess for the first time how confidently these measurements distinguish between the three possible morphologies. As we discuss in detail, morphological classification is related to (but not strictly dependent on) the accuracy with which we can measure the angle $\Delta\Phi$ between the projection of the two spins on the orbital plane. On physical grounds, morphological classification is far more robust: while $\Delta\Phi$ changes on the precession timescale, a binary's morphology only changes on the inspiral timescale.

The paper is organized as follows. In Section II we briefly review GW parameter estimation, the specific grid of binaries examined for this work and the parameters needed to interpret the posterior distribution in the context of post-Newtonian resonances. In Section III we show that the morphology of exactly resonant binaries can be reliably determined at astrophysically plausible signal amplitudes, unless the binary is face-on. Motivated by a recent analytic solution of the spin precession equations [22, 23], we introduce two coordinate sys-

tems to more naturally characterize how well properties of double-spin binaries have been constrained. We conclude in Section IV describing how our results impact the broader program of astrophysical inference using GW measurements. In an attempt to keep this paper self-contained, we report various technical material in the appendices. Appendix A describes the relationship between several conventions used to describe precessing spins that have appeared in the literature. Appendix B reviews the characteristic precession timescales introduced in our previous work on analytic solution of the two-spin precession equations [22, 23]. Finally, in Appendix C we provide some technical details on our parameter estimation procedure.

II. METHODS

A. Candidate sources and signals

The GW signal from the binary depends on 8 intrinsic (physical) parameters – the component masses m_1 and m_2 and spin vectors $\mathbf{S}_1$, $\mathbf{S}_2$ (3 components each) – and 7 extrinsic parameters – the event time $t_{\rm ref}$; luminosity distance D_L; sky location or propagation direction relative to the Earth's equatorial coordinate system, expressed via two angles α, δ (right ascension and declination); and three Euler angles describing the orientation of the binary relative to the Earth. The rotation relating the Earth frame and the binary's frame is commonly characterized using the line of sight $\hat{\mathbf{N}}$ from the observer to the binary and the time-dependent orbital angular momentum direction $\hat{\mathbf{L}}$, evaluated at some fiducial orbital frequency. For example, the orbital orientation is often characterized by the inclination angle ι, defined by $\cos\iota = -\hat{\mathbf{L}}\cdot\hat{\mathbf{N}}$ (in this convention, a binary whose angular momentum points towards the observer corresponds to $\iota = 0$.) Among different possible parametrizations for these intrinsic and extrinsic parameters, we choose to use the following [39]:

$$\boldsymbol{\theta} = \{m_1, m_2, \chi_1, \chi_2, \theta_{JN}, \theta_{LS_1}, \theta_{LS_2}, \Delta\Phi, \phi_{JL}\}, \quad (1)$$

as well as coalescence event's 4 spacetime coordinates, polarization, and orbital phase, which will be marginalized over and not discussed henceforth. In this list, the symbol m_i denotes the component masses, $\chi_i = |\mathbf{S_i}|/m_i^2$ the adimensional spin magnitudes, θ_{LS_i} the angle between the orbital angular momentum $\mathbf{L}$ and the spin vector $\mathbf{S}_i$, θ_{JN} the angle between the total angular momentum $\mathbf{J} = \mathbf{L} + \mathbf{S}_1 + \mathbf{S}_2$ and the line of sight to the observer $(-\hat{\mathbf{N}})$, $\Delta\Phi$ the azimuthal angle between $\mathbf{S}_1$ and $\mathbf{S}_2$, and ϕ_{JL} the azimuthal angle between $\mathbf{J}$ and $\mathbf{L}$, relative to a reference phase defined via the projection of $-\hat{N}$ onto the orbital plane; see Figure 1 and [39]. All parameters are specified when the GW frequency (twice the orbital frequency) is $f_{\rm ref} = 100$Hz. Except for m_1, m_2, χ_1, χ_2, all of our intrinsic parameters evolve during the inspiral.
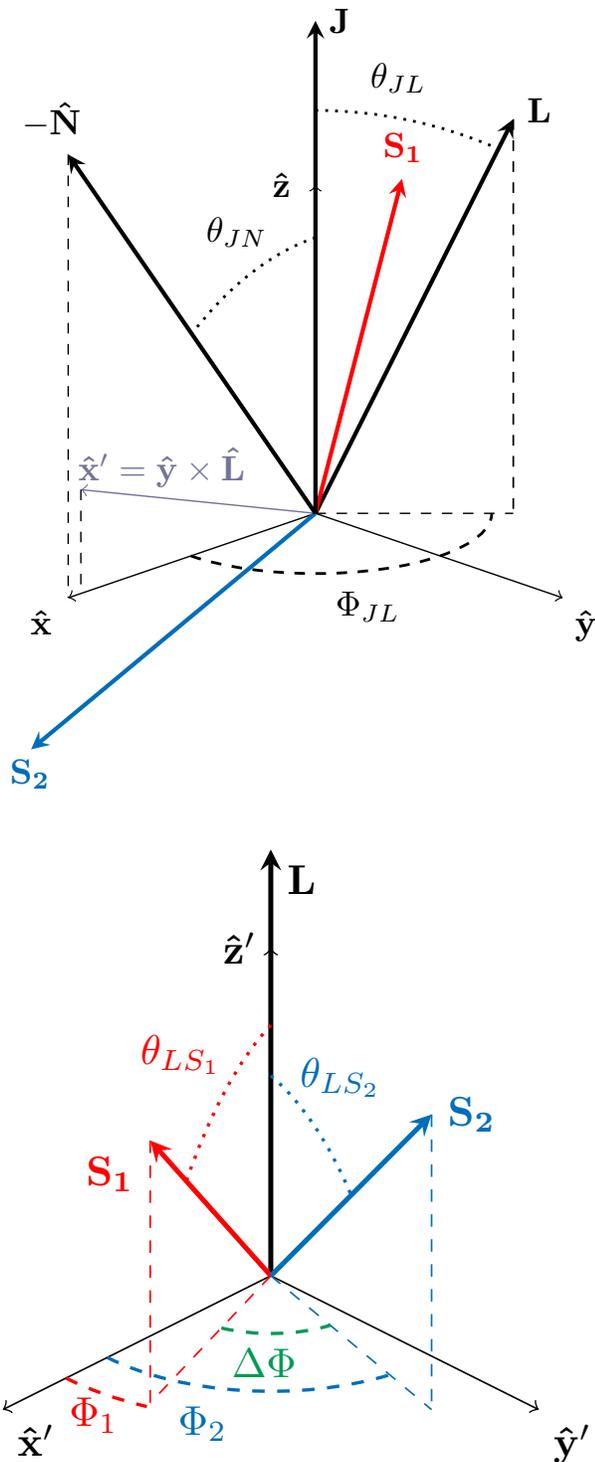
FIG. 1. Definitions of the angles used throughout this paper. The directions of the spins $\mathbf{S}_1$ and $\mathbf{S}_2$ are specified using polar angles θ_{LS_i} and azimuthal angles Φ_i ($i = 1, 2$), measured relative to $\hat{\mathbf{x}}' = \hat{\mathbf{x}} \times \hat{\mathbf{L}}$. For resonant binaries, the orbital angular momentum and spins remain coplanar, implying that the angle $\Delta\Phi = \Phi_2 - \Phi_1$ remains constant: either $\Delta\Phi = 0$ or $\Delta\Phi = \pi$.

The orbital dynamics and GW signal are constructed via the LALSIMULATION SpinTaylorT4 code [51]. Based on previous implementations [52, 53], this time-domain code solves the orbital dynamics of an adiabatic, quasi-circular inspiraling binary using the "TaylorT4" method [54] for the phase evolution and (orbit-averaged) precession equations for the angular momenta [19]. In all cases we used a gravitational wave phase up to 3.5PN in non-spinning; up to 2.5PN in spin-orbit terms; up to 2PN spin-spin terms; and orbit-averaged spin precession equations up to 2PN, including the leading-order spin-orbit and spin-spin interactions. As described below, we performed calculations both with and without black hole-consistent coefficients in composition-dependent terms like the quadrupole-monopole (QM) coupling. We evaluate the GW amplitude $h(t)$ using only the leading-order (Newtonian) quadrupole [55].

To compare waveforms from binaries belonging to different morphologies in controlled conditions we investigate only a specific combination of the binaries' intrinsic parameters: total mass $M = 13.5 M_\odot$, mass ratio $q = m_2/m_1 = 0.8$ (which implies $m_2 = 6.0 M_\odot$ and $m_1 = 7.5 M_\odot$), and adimensional spin magnitudes $\chi_1 = \chi_2 = 1$ (maximally spinning BHs). Our choice, motivated by population-synthesis predictions [2–4] and computational restrictions[1], also facilitates comparisons with our previous works [24, 49].

Following [49], we parametrize binaries from each morphology using the dimensionless projected effective spin ξ:

$$\xi \equiv \left.\frac{\mathbf{S}_0 \cdot \hat{\mathbf{L}}}{M^2}\right|_{f=f_{\mathrm{ref}}} = \frac{\chi_1 \cos\theta_{LS_1} + q\,\chi_2 \cos\theta_{LS_2}}{1+q} \quad (2)$$

where $\mathbf{S}_0$ is the effective spin

$$\mathbf{S}_0 \equiv (1+q)\,\mathbf{S}_1 + \left(1 + \frac{1}{q}\right)\mathbf{S}_2 \,. \quad (3)$$

The projected effective spin ξ, which was first introduced in [56, 57] and used to solve the spin precession equations in [22, 23], is a constant of motion at 2PN order in spin precession and 2.5PN order in radiation reaction.

Our candidate sources will be exactly resonant, which is a conservative choice, since in this case the waveforms are weakly modulated and our ability to constrain parameters correlates with the modulation in the waveforms. For resonant binaries, for each ξ and each family there are unique values of $\theta_{LS_1}, \theta_{LS_2}, \Delta\Phi$, meaning that $(\xi, \Delta\Phi)$ uniquely label the source. For simplicity, we fix $\phi_{JL} = 0$ at $f_{\mathrm{ref}} = 100\mathrm{Hz}$, so $\hat{\mathbf{N}}, \mathbf{L}, \mathbf{J}$ are coplanar. Finally, because the amount of spin-induced precession seen by the observer in the GW signal depends on θ_{JN} [49], we explore a range of θ_{JN} between 0 and $\pi/2$ without loss

---

[1] Data presented in this paper involves full MCMC simulations which required several million CPU hours over the course of several months to compute.

Parameter	Value(s)
m_1	$7.5\ M_\odot$
m_2	$6\ M_\odot$
χ_1	1.0
χ_2	1.0
L/M^2	0.896
$\Delta\Phi$	$0,\ \pi$
ξ	-1, -0.9, ..., 1
θ_{JN}	$0, \frac{\pi}{8}, \frac{\pi}{4}, \frac{3\pi}{8}, \frac{\pi}{2}$

TABLE I. **Overview of simulated binaries.** Input binary parameters at $f = 100$Hz (equivalent to $v = \sqrt{\pi f \mathcal{M}} \simeq 0.208$, where $\mathcal{M} \equiv (m_1 m_2)^{3/5}/(m_1 + m_2)^{1/5}$ is the chirp mass) for the $2 \times 21 \times 5$ distinct parameter estimation calculations described in the text.

of generality: the posterior distribution for sources with $\theta_{JN} > \pi/2$ can be related to a posterior with $\theta_{JN} < \pi/2$ by suitable reflection symmetry. Hence, having chosen the resonant family ($\Delta\Phi = 0$ or $\Delta\Phi = \pi$); the inclination angle θ_{JN} (0, $\pi/8$, $\pi/4$, $3\pi/8$, $\pi/2$); and ξ in the $[-1, 1]$ interval in steps of 0.1, we obtain 42 candidate sources and 210 candidate signals.

For simplicity we adopt the sky location $(\alpha, \delta) = (0°, 0°)$ and fiducial GPS time equal to zero. To better isolate the intrinsic differences between these signals, we require all sources to produce the same coherent amplitude in a network consisting of the three (two Advanced LIGO plus Virgo) interferometers, using the design sensitivity curves [58]. Specifically, we select the distance for each source such that the network signal-to-noise ratio (SNR) is 20, a high but not unreasonable value for first detections [1, 59, 60].

This procedure defines two families of candidate sources, one for $\Delta\Phi = 0$ and one for $\Delta\Phi = \pi$, each of which is characterized by two parameters (ξ, defined in Eq. 2, and θ_{JN}), and produces a well-defined strain response in each idealized instrument. For all masses and spins, the family with $\Delta\Phi = \pi$ has a special point $\xi = \xi_T \equiv (\chi_1 - q\chi_2)/(1+q)$ such that both spins are parallel to the orbital angular momentum and antialigned with respect to one another, i.e. $(\theta_{LS_1}, \theta_{LS_2}) = (\pi, 0)$ [61]. For our choice of binary parameters, $\xi_T \simeq -0.11$ [see Eq. (2) and Figure 2].

Rather than explore an ensemble of noise realizations, following previous studies [38, 47, 62] we adopt a unique preferred noise realization (exactly zero noise) for all simulations and all instruments; see Appendix C for details. As discussed below, we have repeated parts of the analysis using randomly selected detector noise to demonstrate that our results are robust with respect to this choice. Simulation properties are summarized briefly in Table I; in the Appendix, Table II provides an explicit list, including derived parameters (such as J and the termination frequency).

As reviewed at length in [49], each one-parameter family of resonances has distinctly different angular momenta orientations as a function of ξ: in other words, varying ξ significantly changes the dynamics of the source bi-

nary. For example, as shown in the left panel of Figure 2, our one-parameter family of dynamically unique binaries with $\Delta\Phi = 0$ has both spins comparably ($\cos\theta_{LS_1} \simeq \cos\theta_{LS_2}$) and often significantly misaligned with $\mathbf{L}$. As a result, the $\Delta\Phi = 0$ binaries have significant misalignment between $\mathbf{L}$ and $\mathbf{J}$, as seen in the right panel of Figure 2. By contrast, our family of $\Delta\Phi = \pi$ sources all have either one or the other spin nearly aligned with the orbital angular momentum: $\cos\theta_{LS_2} \simeq 1$ for $\xi > \xi_T$ and $\cos\theta_{LS_1} \simeq -1$ for $\xi < \xi_T$. As shown in the right panel of Fig. 2, our $\Delta\Phi = \pi$ binaries have minimal misalignment between $\mathbf{L}$ and $\mathbf{J}$, particularly when $\xi < \xi_T$. We will see below that some measurements are strongly correlated with the amplitude of precession-induced modulations, and therefore correlate strongly with the misalignment angle $\theta_{JL}(\xi) = \arccos \hat{\mathbf{J}} \cdot \hat{\mathbf{L}}$. Note also that, for our simulations, the values $\xi = \pm 1$ correspond to spin-aligned, non-precessing binaries.

The quadrupole-monopole term

Consistent with all previous parameter estimation studies and the implementation of LALSIMULATION at the time this project began, our spin precession equations explicitly omitted the QM coupling described in [57]. After realizing the omission, we have added the missing terms to the LALSIMULATION code, and we have repeated parts of our computationally expensive analysis including the QM interaction. The conclusions of this exercise are encouraging, and our main results are very robust under perturbations: as discussed in Sec. III F below, the posterior distributions obtained with and without the QM interaction are basically indistinguishable, at least for near-resonant binaries.

The omission of the QM term has several important consequences from a theoretical point of view: (i) The projected effective spin ξ is only approximately conserved in our simulated binaries. If ξ is not conserved, spin precession in general will not be quasi-periodic. Fortunately, as argued in Sec. III F below, ξ is nearly conserved even in the absence of the QM interaction for near-resonant binaries, so this does not have a dramatic impact on the present analysis, but the omission of the QM interaction could have larger effects for binaries that are far from resonance. To eliminate any ambiguity, ξ (like all spin-dependent intrinsic parameters) must be evaluated at some reference frequency, here chosen to be 100Hz. (ii) The morphological classification described in [22, 23] is no longer exact: for example, binaries that should be exactly resonant can, in practice, perform small librations around resonant configurations, and some binaries may not belong to any of the three morphologies discussed in [22, 23]. (iii) Precessional dynamics is obviously modified at 2PN, and so is the evolution of the binary on the radiation-reaction timescale.
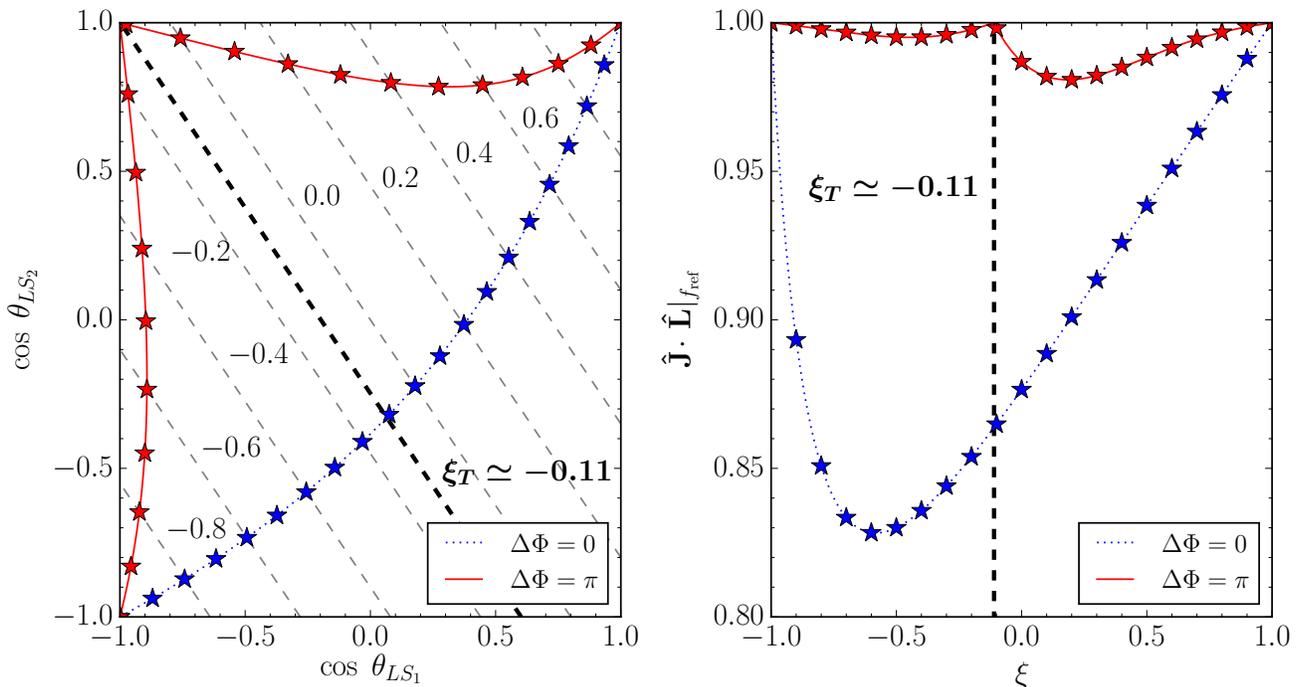
FIG. 2. **Review of resonant dynamics and our simulations.** *Left panel*: Illustration of the specific two one-parameter families of resonant binaries used in this work. The two curved paths show $\cos\theta_{LS_1}, \cos\theta_{LS_2}$ for $\Delta\Phi = 0$ (blue and dotted) and $\Delta\Phi = \pi$ (red and solid), superimposed on contours of constant ξ (dashed). $\xi = \xi_T \simeq -0.11$ is shown with a thick dashed line. Stars mark the location of each of our simulations (blue for $\Delta\Phi = 0$, red for $\Delta\Phi = \pi$). *Right panel*: Plot of $\hat{\mathbf{J}} \cdot \hat{\mathbf{L}}$ versus ξ for each resonant family at the reference frequency $f_{\rm ref} = 100$ Hz. As discussed in the text, our source binaries in the $\Delta\Phi = \pi$ resonance have spins and $\mathbf{L}$ much more closely aligned with each other than sources in the $\Delta\Phi = 0$ resonance. All source binaries have $L > S_1 + S_2$, and hence dynamics characterized by the two-spin solution described in [22, 23].

B. Gravitational wave parameter estimation for double-spin binaries

Parameter estimation can be performed using Bayes' theorem: a prior probability distribution $p(\theta|\mathcal{H})$ (where $\mathcal{H}$ is the hypothesis and θ represents collectively the parameters of the system) is updated upon receiving data d from the experiment to give a posterior distribution $p(\theta|d, \mathcal{H})$

$$p(\theta|d, \mathcal{H}) = \frac{p(\theta|\mathcal{H})p(d|\theta, \mathcal{H})}{p(d|\mathcal{H})}, \tag{4}$$

where $p(d|\theta, \mathcal{H})$ is called the "likelihood". Starting from an appropriate prior distribution, samples of the posterior distribution are randomly selected through a stochastic sampler using information from the data. We perform parameter estimation on simulated GW signals from resonant binaries using the LALINFERENCE suite [48], in the LALINFERENCE_MCMC implementation. This Markov Chain Monte Carlo (MCMC) algorithm generates a series of independent samples from the posterior distribution, given prior probabilities for all physical parameters. Consistent with previous work [48], we a priori assume component masses are uniformly distributed between $1M_\odot$ and $30M_\odot$, with total mass less than $35M_\odot$;

component spins randomly oriented, with uniformly distributed amplitude; and the merger event occurs within ± 0.1s of our proposed event time $t_{\rm ref}$. To account for the high mass of our candidate sources and the high sensitivity of the advanced instruments used in this study, we allow the physical position to be uniformly distributed on a sphere of Euclidean radius 6Gpc, implying uniformity over the sky and in distance – i.e., $p(d) \propto d^2$ – out to 6Gpc. The prior was not modified to model selection bias. This prior includes extremely high mass ratios and a wide range of spins, favoring binaries dominated by a single spin rather than systems showing strong two-spin effects; our conclusions drawn using this unfavorable and astrophysically unmotivated prior should therefore be taken as conservative underestimates. For simplicity and consistent with previous work, cosmological effects are not included in our calculations.[2] Finally, we stop our calculations when the final Markov Chain, after

———

[2] The most distant sources in our sample, with $\theta_{JN} \simeq 0$ and $\xi \simeq \pm 1$, were placed at $d_L \simeq 815$Mpc, or $z \simeq 0.2$ with current cosmological parameters; typical sources have $d_L \simeq 500$Mpc, or $z \simeq 0.12$. Because the GW strain depends only on the redshifted masses, the posterior including cosmological effects can be derived from a cosmology-free posterior by a coordinate transfor-
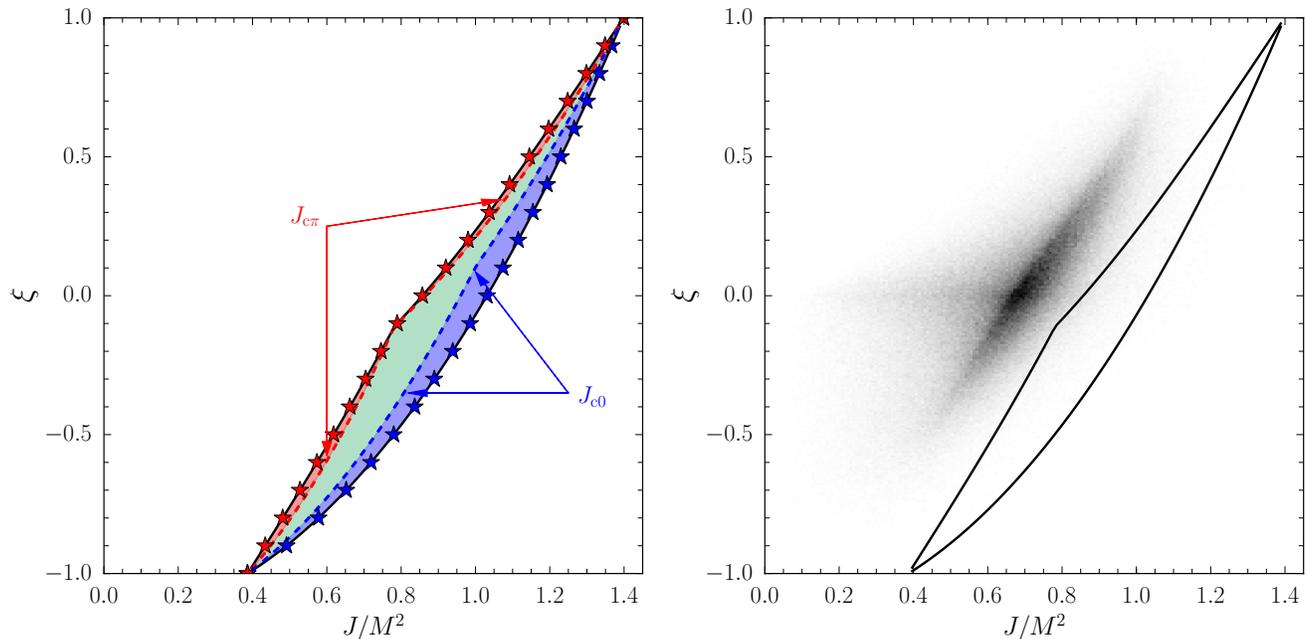
FIG. 3. **The $J\xi$-plane.** For fixed source parameters m_1, m_2, χ_1, χ_2 and f_{ref}, the solid black lines indicate the extent of the allowed values of J and ξ. Any point on the lower (upper) edge of this region corresponds to a $\Delta\Phi = 0$ ($\Delta\Phi = \pi$) post-Newtonian resonance. The specific parameter configurations used in this paper are illustrated by red stars (on the upper boundary) and blue stars (on the lower boundary), as in Figure 2. *Left:* For these same fixed source parameters, three shaded regions (red on top; blue on the bottom; and green in between) show the regions for, respectively, librating about $\Delta\Phi = \pi$, about $\Delta\Phi = 0$, and circulating precession morphologies (described in the text). Dashed lines separating these regions (marked by arrows) show morphology boundaries $J_{c0,c\pi}(\xi)$. *Right:* Prior probability $p(J, \xi)$, derived from the priors described in II B by marginalizing out m_1, m_2, χ_1, χ_2. For scale, the black curve also shows the same boundary of allowed (J, ξ) values shown in the left panel. The structure in this distribution reflects the broad range of mass ratios and spin orientations included in the prior; see the text for details.

downsampling to remove correlations, has roughly 2,000 uncorrelated samples from the posterior [48].

The parameters of the posterior samples can be represented in any coordinate system, allowing us to efficiently compute the posterior $p(\theta)$ using *any* parameters θ, independent of the coordinates used internally by the MCMC simulation. The relative orientation of the two spins with respect to the orbital angular momentum, θ_{LS_1} and θ_{LS_2}, can be used to characterize the system. Motivated by the analysis of [22, 23] and as described at greater length in Appendix A, we replace these angular variables with (J, ξ), where ξ is given by Eq. (2) and

$$
J = \big[L^2 + S_1^2 + S_2^2 + LS_1 \cos\theta_{LS_1} + LS_2 \cos\theta_{LS_2}
$$
$$
+ 2S_1 S_2 \left(\sin\theta_{LS_1} \sin\theta_{LS_2} \cos\Delta\Phi + \cos\theta_{LS_1} \cos\theta_{LS_2} \right) \big]^{\frac{1}{2}}
\tag{5}
$$

is the magnitude of the total angular momentum, $J = |\mathbf{J}|$. For each resonant family ($\Delta\Phi = 0, \pi$), each pair

---

mation, using a modified (Euclidean) distance prior rather than one consistent with cosmology. At the distances of interest, a Euclidean and cosmological distance prior nearly agree.

(J, ξ) uniquely specifies the binary configuration (see Fig. 3). The magnitude $L \equiv |\mathbf{L}|$ of the orbital angular momentum is calculated at leading (Newtonian) order: $L = \eta M^2/v = \eta M^2/(\pi f_{\text{ref}} M)^{1/3}$. Unlike the system-frame parameters described above, these parameters naturally reflect the separation of timescales in the two-spin problem, with ξ conserved up to 2PN order on all timescales by the orbit-averaged spin-precession equations; J changing on the radiation-reaction timescale; and $\Delta\Phi$ changing on the precession timescale [22, 23]. For each fixed m_1, m_2, χ_1, χ_2 and f_{ref}, a range of (J, ξ) is allowed; see Gerosa *et al.* [23] for details. For single-spin binaries, the relationship between J and ξ at fixed L is one-to-one; for double-spin binaries, a range of J are allowed at each fixed ξ. To guide the eye in the plots that follow, we evaluate and show this "allowed" region in the $J\xi$-plane for the chosen source parameters m_1, m_2, χ_1, χ_2 in Figure 3. We will use $J_{r0}(\xi), J_{r\pi}(\xi)$ to denote the maximum and minimum values of J for a given ξ. Points on these two curves, including the injections described above, are all resonant binaries: binaries with $J = J_{r\pi}(\xi)$ belong to the $\Delta\Phi = \pi$ resonance, while those with $J = J_{r0}(\xi)$ belong to the $\Delta\Phi = 0$ resonance.

Additionally, as described in Refs. [22] and [23], these parameters facilitate *morphological classification*, sub-

dividing the parameter space $\mathcal{H}$ into three disjoint regions $\mathcal{H}_0, \mathcal{H}_C, \mathcal{H}_\pi$, set by the (nondissipative) dynamics at $f_{\mathrm{ref}} = 100$Hz. Specifically, $\mathcal{H}_0$ and $\mathcal{H}_\pi$ are the systems whose spins are librating about the $\Delta\Phi = 0$ and $\Delta\Phi = \pi$ resonance, respectively; $\mathcal{H}_C$ are the remaining, circulating binaries. Geometrically, these three regions are separated by configurations where either $\mathbf{S}_1$ or $\mathbf{S}_2$ are parallel to $\mathbf{L}$ at some point during one precession cycle. From a computational point of view, motivated by [22, 23], at each m_1, m_2, χ_1, χ_2 we determine the morphology from the values of J and ξ at 100 Hz. We define $J_{c0}(\xi), J_{c\pi}(\xi)$ as the two values of J which allow either $\mathbf{S}_1$ or $\mathbf{S}_2$ to be parallel to $\mathbf{L}$ at some point during their precession cycle, ordered as $J_{r\pi}(\xi) < J_{c\pi}(\xi) < J_{c0}(\xi) < J_{r0}(\xi)$. Because these surfaces separate the different morphologies, we identify the appropriate morphology simply by comparing J to $J_{c0,c\pi}(\xi)$: binaries with $J < J_{c\pi}(\xi)$ belong to $\mathcal{H}_\pi$; binaries with $J > J_{c0}(\xi)$ belong to $\mathcal{H}_0$; and binaries with $J_{c\pi} < J < J_{c0}$ belong to $\mathcal{H}_C$. These boundaries are illustrated in Figure 3.

We apply morphological decomposition to the list of posterior samples, classifying the fraction $p(A)$ of samples that are consistent with each morphology $A = \mathcal{H}_0$, $\mathcal{H}_\pi$, and $\mathcal{H}_C$, respectively. As described in previous work (see in particular [22, 23]), while librating binaries occur frequently near merger for comparable-mass binaries, a relatively small amount of the possible parameter space describing all compact binaries corresponds to librating orbits trapped near a resonance ($\mathcal{H}_{\pi,0}$), as opposed to circulating orbits ($\mathcal{H}_C$).

Using the prior parameter distribution described below Eq. (4),[3] we find prior probabilities $p_{\mathrm{prior}}(\mathcal{H}_{0,\pi,C})$

$$
\begin{aligned}
p_{\mathrm{prior}}(\mathcal{H}_0) &= 0.118\,; \\
p_{\mathrm{prior}}(\mathcal{H}_\pi) &= 0.049\,; \\
p_{\mathrm{prior}}(\mathcal{H}_C) &= 0.832\,.
\end{aligned}
\tag{6}
$$

The prior also implies a marginal distribution $p(J, \xi)$, shown in the right panel of Figure 3. The marginal distribution has several salient features, most notably a peak near $(J, \xi) \simeq (0.6, 0)$ arising for example from randomly-oriented spins in unequal-mass binary black holes. Extending away from that peak are three wedges, corresponding to binaries (a) with spins increasingly aligned with $\mathbf{L}$, extending upward toward $J \simeq 1$ and $\xi \simeq 1$; (b) with spins increasingly anti-aligned with $\mathbf{L}$, extending downward towards $\xi \simeq -1$; and (c) a region extending

---

[3] To ensure consistency, we draw samples from the prior by running the parameter estimation code with input $h(t) = 0$. While we are forced to adopt the ad-hoc choices of Eq. (6) for prior probabilities to be consistent with the mass and mass ratio distribution described previously and used by convention in LALIN-FERENCE, we emphasize that those probability distributions were chosen arbitrarily to avoid the impression of bias in mass. Nature likely favors other mass distributions [2–4], which may further enhance the prior probability that non-circulating morphologies occur.

to the left along $\xi \simeq 0$ with small J, corresponding for example to small mass ratios q and small primary spins χ_1.

The posterior distribution can also be parametrized using the two frequencies implied by the spin precession equations, evaluated (to avoid ambiguity) using a reference orbital frequency: here $f_{\mathrm{ref}} = 2f_{\mathrm{orb}} = 100$Hz. These two timescales appear directly in the spin and orbital dynamics, and hence are reflected in the waveform. Rather than adopt a precession-phase dependent definition of these two timescales via, e.g., the vector $\mathbf{\Omega}_i$ that appear in the spin precession equations $d\mathbf{S}_i/dt = \mathbf{\Omega}_i \times \mathbf{S}_i$, following Kesden *et al.* [22], Gerosa *et al.* [23] we use an analytic, explicitly doubly periodic solution for the nondissipative precession dynamics to identify a precession timescale τ for the relative spin motion [defined below Eq. (8) in [22]] and a precession frequency $\langle\Omega_z\rangle$ for the motion of $\mathbf{L}$ around $\mathbf{J}$. Relative to their notation, $\langle\Omega_z\rangle \equiv \alpha/\tau$, where α is the precession angle of $\mathbf{L}$ around $\mathbf{J}$ in one spin precession period τ; see Appendix B for details.

III. RESULTS

A. Robust morphological classification

Let us first consider sources with $\Delta\Phi = 0$. Except for binaries that are either face-on ($\theta_{JN} = 0$) or have both spins nearly aligned with $\mathbf{L}$ ($|\cos\theta_{LS_1}| \simeq 1$ and $|\cos\theta_{LS_2}| \simeq 1$), our calculations show that the posterior probability $p(\mathcal{H}_0)$ is a good indicator of which resonant family the source came from, for almost all source orientations and ξ, and for astrophysically plausible source amplitudes. For example, the left panel of Figure 4 shows the posterior probability $p(\mathcal{H}_0|\Delta\Phi = 0, \xi, \theta_{JN})$: the fraction of posterior probability implying the source librates about the $\Delta\Phi = 0$ resonance, as a function of the true source parameters (ξ, θ_{JN}) at a fixed source amplitude SNR = 20. This probability is large (and nearly unity) for almost all (ξ, θ_{JN}). For binaries at or near the $\Delta\Phi = 0$ resonance, we can confidently classify them in their corresponding resonant regime. Equally striking, the center-left panel shows that the probability of misidentification in the opposite resonance is nearly zero: $p(\mathcal{H}_\pi|\Delta\Phi = 0, \xi, \theta_{JN}) \simeq 0$. These high probabilities should be sharply contrasted with the small prior probability associated with the $\Delta\Phi = 0$ resonance [$p_{\mathrm{prior}}(\mathcal{H}_0) = 0.118$], as the majority of phase space is associated with circulating binaries.

The right panels of Figure 4 show our corresponding but qualitatively different results using source binaries from the $\Delta\Phi = \pi$ resonant family. Except for specific configurations, our calculations show that the posterior probability favors the circulating morphology and disfavors the "incorrect" classification. This follows from geometrical considerations: $\Delta\Phi = \pi$ sources are more aligned and precess less, making them more difficult to

FIG. 4. **Constraining morphology versus inclination: the posterior.** Classification probability versus ξ for different values of θ_{JN} at fixed SNR = 20. Panels in this plot are organized as a matrix: sources ($\Delta\Phi = 0$ or $\Delta\Phi = \pi$) are columns; the fraction of the posterior in each morphology ($\mathcal{H}_0, \mathcal{H}_\pi, \mathcal{H}_C$) are rows; and each panel shows the corresponding probability evaluated for sources at different values of ξ. For example, the bottom-left panel shows the probability $p(\mathcal{H}_C|\Delta\Phi = 0)$ versus ξ and (in different line styles) versus θ_{JN}. Nearly aligned binaries ($\xi \simeq 1, -1$ or $\Delta\Phi = \pi$ and $\xi = \xi_T \simeq -0.11$) and nearly face-on binaries ($\theta_{JN} \simeq 0$) cannot be reliably classified (top left and middle right). A source with $\Delta\Phi = 0$ can be reliably classified in the $\mathcal{H}_0$ morphology (top left) unless face-on (for our simulations, $\xi \approx \pm 1$); however, a source with $\Delta\Phi = \pi$ can be reliably classified in the $\mathcal{H}_\pi$ morphology only if $\theta_{JN} \simeq \pi/2$ and $\xi \neq -1, 1, \xi_T$ (green curve in middle right). In other words, cases where the probabilities vary significantly with ξ reflect how the misalignment angles between the various angular momenta change versus ξ: compare to Figure 2. Due to the relatively small number ($N \simeq 2000$) of posterior samples used, these probabilities have a few percent (binomially distributed) sampling uncertainty.
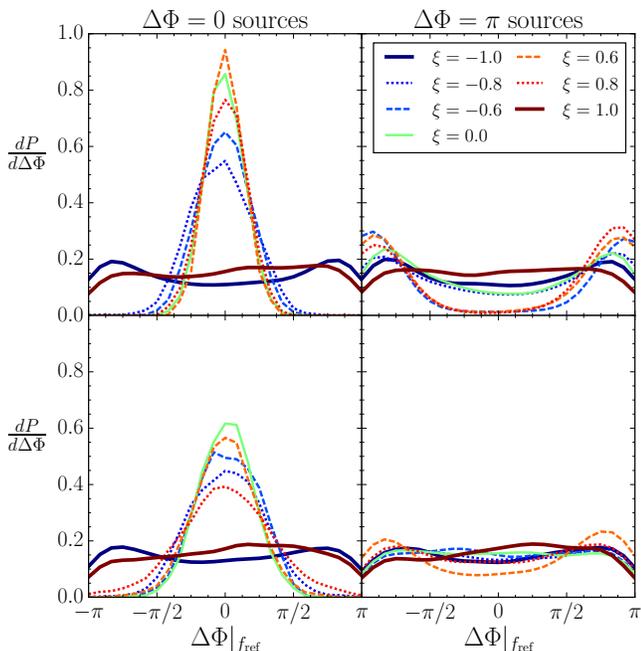
FIG. 5. **Constraining $\Delta\Phi$ at** 100 Hz. Probability distribution $dP/d\Delta\Phi$ of the phase angle $\Delta\Phi$ between the spins can be reliably measured for $\Delta\Phi \simeq 0$. Plot shows the posterior distribution for $\Delta\Phi$ between the spins using spin vectors at the reference frequency $f_{\rm ref} = 100$ Hz, given data containing sources with $\Delta\Phi = 0$ (left column) or $\Delta\Phi = \pi$ (right column), with either $\theta_{JN} = \pi/2$ (top) or $\theta_{JN} = \pi/4$ (bottom). In all panels, colors indicate different values of ξ, as shown in the legend. This figure shows that the posterior distribution in the intrinsic parameter $\Delta\Phi$ depends strongly on the extrinsic parameter θ_{JN} and weakly on the intrinsic parameter ξ, except for nearly aligned systems $\xi \simeq \pm 1$.

distinguish from non-precessing sources. The probability of "correct" classification $p(\mathcal{H}_\pi|\Delta\Phi = \pi, \xi, \theta_{JN})$ shown in the middle-right panel decreases significantly at $\xi = \xi_T \simeq -0.11$. This value of ξ corresponds to a special configuration featured by $\Delta\Phi = \pi$ sources, with $\cos\theta_{LS_1} = -1$ and $\cos\theta_{LS_2} = 1$; see, e.g., our Figure 2 or Figure 2 of [49]. For our injection masses and spin magnitudes, this "aligned" configuration occurs at $\xi = \xi_T \simeq -0.11$, as explained earlier.[4] Resonant binaries at and near ξ_T have spins that barely precess, being almost parallel to $\mathbf{L}$. In other words, just like the two limits $\xi \to 1$ and $\xi \to -1$,

when both spins are coaligned with each other and $\mathbf{L}$, resonant sources with $\Delta\Phi = \pi$ and $\xi \simeq \xi_T$ have almost indistinguishable dynamics from a *non-precessing* binary. As seen in Figure 4, for sources with $\xi \simeq \xi_T$ and $\Delta\Phi = \pi$ the morphology is only weakly constrained by observation: $p(\mathcal{H}_\pi|\Delta\Phi = \pi, -0.11, \theta_{JN})$ is small, comparable to the prior (see Sec. III E and Fig. 12 below). Second, the probability for correct classification of a $\Delta\Phi = \pi$ source is often significantly smaller than the corresponding $\Delta\Phi = 0$ result. As emphasized in [49], the $\Delta\Phi = \pi$ and $\Delta\Phi = 0$ resonant families have qualitatively different dynamics and GW signals: $\Delta\Phi = \pi$ resonances undergo substantially less precession of $\mathbf{L}$, and hence have less modulated GWs. As a result, at fixed signal amplitude, GW measurements of sources from the $\Delta\Phi = \pi$ resonance should be less effective at measuring double-spin physics like the morphology, implying the lower probabilities $p(\mathcal{H}_\pi|\Delta\Phi = \pi, \xi, \theta_{JN}) \lesssim p(\mathcal{H}_0|\Delta\Phi = 0, \xi, \theta_{JN})$ seen in the corresponding panels of Figure 4.

To qualitatively corroborate this analysis, we also examined the posterior for $\Delta\Phi$; an example appears in Figure 5. In most cases, $\Delta\Phi$ could be weakly constrained to be $\simeq 0$ or $\simeq \pi$. By definition, the region $\mathcal{H}_0$ corresponds to libration about the $\Delta\Phi = 0$ resonance. Because the phase-space trajectories in this region explicitly cannot extend to $\Delta\Phi = \pi$ [22, 23], posterior samples in this region explicitly disfavor $\Delta\Phi \simeq \pi$; in fact, depending on ξ, the allowed region of $\Delta\Phi$ can be narrow.[5] To summarize, our ability to confidently classify source morphology to $\mathcal{H}_{0,\pi}$ implies $\Delta\Phi$ can be constrained away from $\pi, 0$, respectively. That said, morphological classification is more robust and qualitatively different than measurements of $\Delta\Phi$; for example, while $\Delta\Phi$ changes on the precession timescale, a binary's morphology only changes on the inspiral timescale.

All of our results depend on the signal amplitude, here fixed at SNR = 20. Repeating parts of our study with much stronger signals (SNR $\simeq 50$), we have found dramatically improved morphological classification, even for sources with $\Delta\Phi = \pi$. Conversely, our ability to reliably classify morphologies gradually degrades at lower source amplitude, as shown in Figure 6.

B. Using conserved quantities as coordinates to describe double-spin measurements

On physical grounds, we expect GW measurements to best constrain quantities that are constant on the longest

---

[4] The spin-aligned configuration at $\xi = \xi_T$ on the $\Delta\Phi = \pi$ family arises because the down/up configuration is a stable fixed point of the spin precession equations; by contrast, for our masses, spin magnitudes, and frequencies, the up/down configuration is unstable and not a member of the $\Delta\Phi = 0$ family [61]. When the up/down configuration is stable, the point with $\cos\theta_1 = +1$ and $\cos\theta_2 = -1$ will belong to the $\Delta\Phi = 0$ resonant family and we anticipate similarly diminished precession amplitudes in its vicinity leading to a similarly difficult challenge in identifying the morphology.

[5] At sufficiently high signal amplitudes, phase angles like $\Delta\Phi$ can be measured directly, independent of how rapidly they evolve with frequency. For example, the phase angle ϕ_{JL} can be estimated to within an angle of order $2\pi/$SNR, with a coefficient that depends on the line of sight (θ_{JN}) and the amplitude of precession of $\mathbf{L}$ around $\mathbf{J}$ (e.g., the characteristic angle between $\mathbf{L}$ and $\mathbf{J}$): see, e.g., [38].
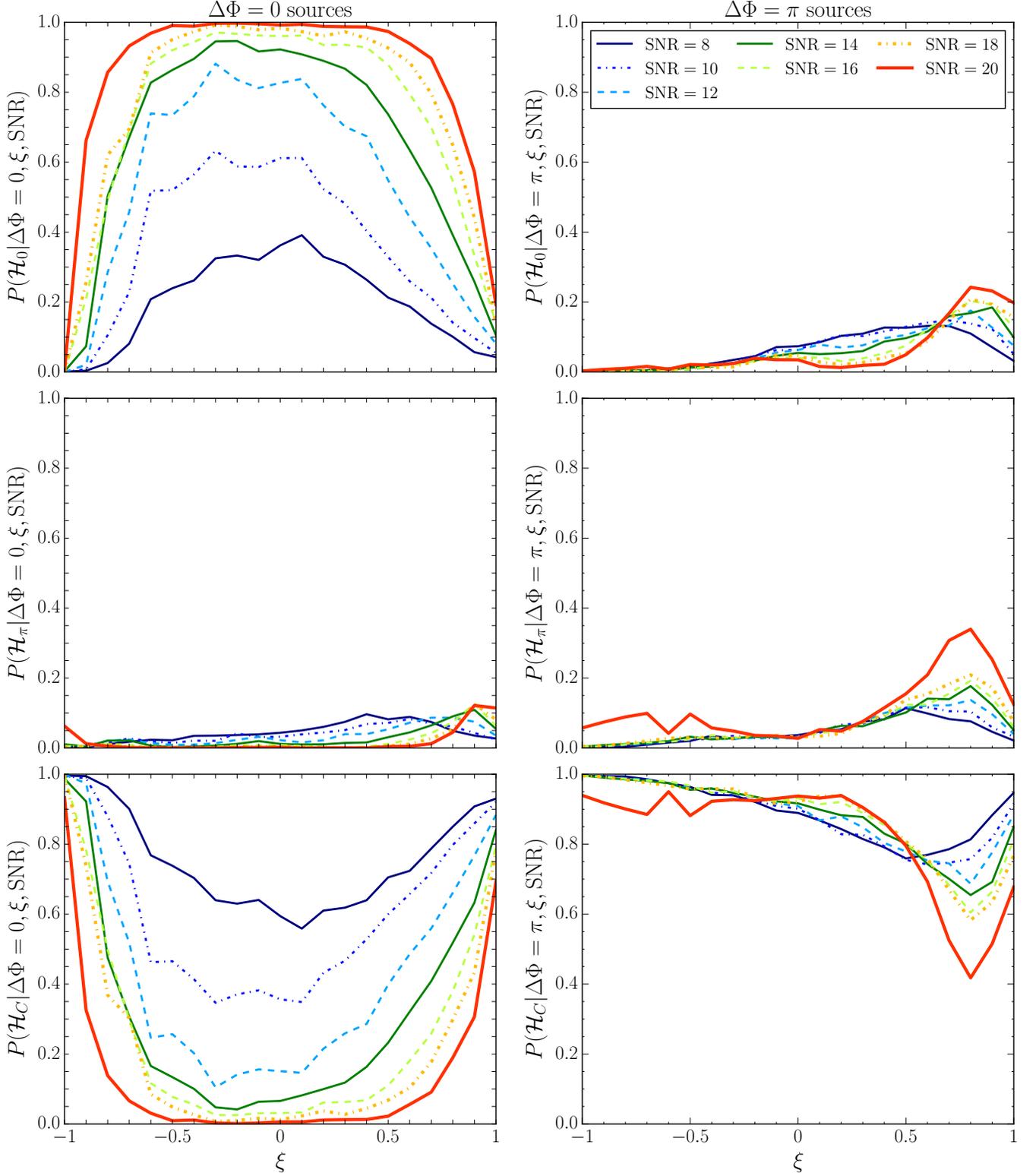
FIG. 6. **Constraining morphology versus SNR.** Plot of the classification probability versus ξ for different choices of SNR and $\theta_{JN} = \pi/4$. The panels in this figure are organized as in Figure 4. As described in Appendix C, the SNR = 20 results (red curve) were produced using a lower starting frequency than results for SNR< 20; this discrepancy is responsible for the slight difference in trend between the right panels' results for SNR=20 versus results for SNR< 20.
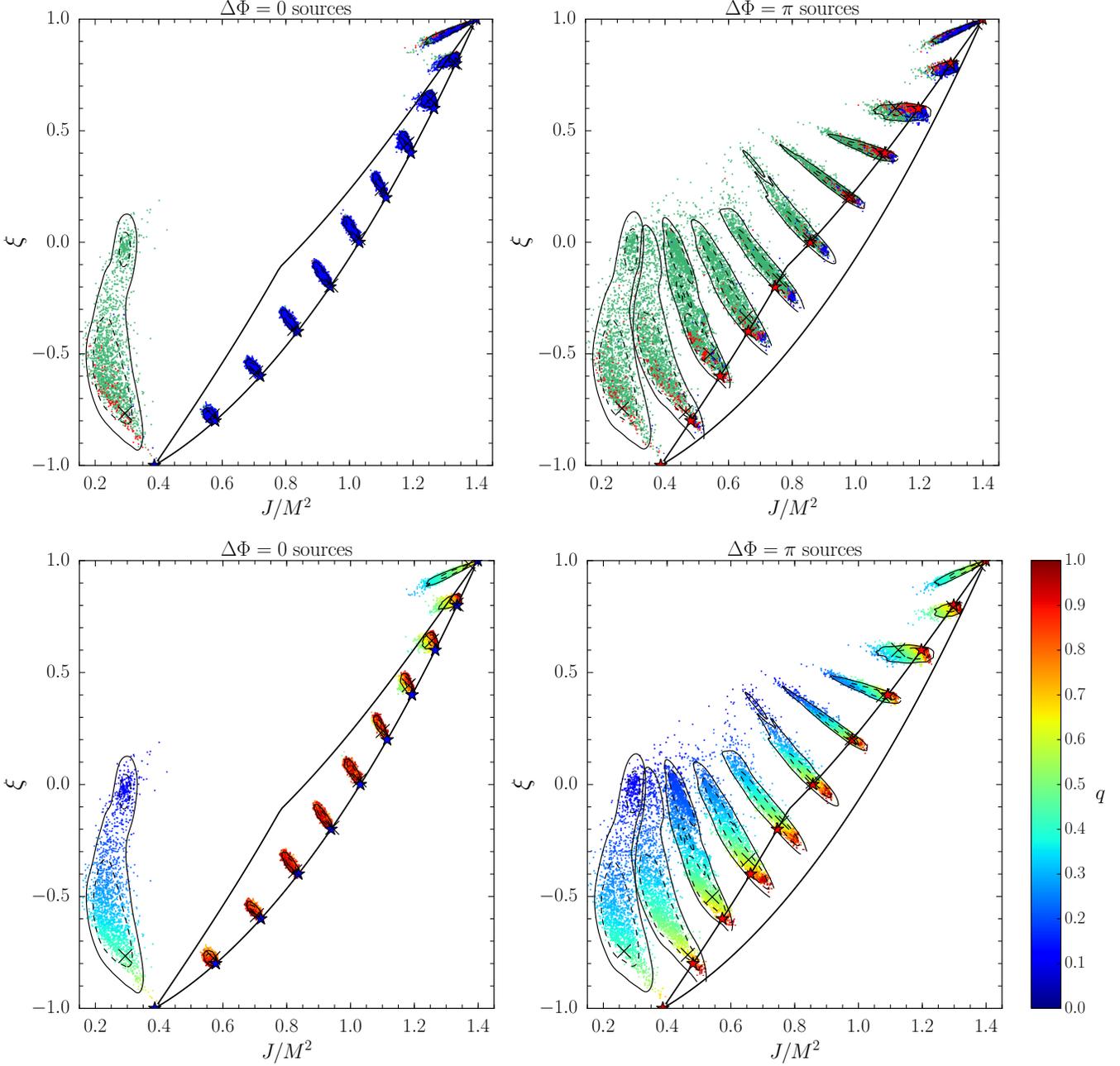
FIG. 7. **Constraining** (J, ξ). The parameters J and ξ can be independently constrained to a narrow volume of parameter space. Posterior distributions from distinct simulations in the $J\xi$-plane for $\theta_{JN} = \pi/4$ and SNR = 20, for source binaries with $\Delta\Phi = 0$ (left) and $\Delta\Phi = \pi$ (right). The actual value from each simulation is marked with a star; the maximum-likelihood estimate is marked by a black cross. To guide the eye, the allowed region for J and ξ for the true source parameters is superimposed (thick black line) as in Figure 3. As the allowed region depends on masses and spins, not all points in the posterior lie in this region; see [23] for details. Solid and dashed black lines show the 95% and 67% confidence intervals for each set of posterior samples from distinct simulations. *Top panels:* Samples are colored according to morphology (blue: librating around $\Delta\Phi = 0$, red: librating around $\Delta\Phi = \pi$, green: circulating). *Bottom panels:* Samples are colored according to the posterior mass ratio q. In our simulations, binaries without sufficiently strong precession-induced modulation to enable tight constraints on q are equally poorly constrained in morphology: our ability to classify morphology correlates with our ability to constrain q.

timescales. In a two-spin system, while the specific component spins and orbital angular momenta depend effectively on a precession phase choice, recent analytic work [22, 23] has identified natural quantities, conserved on the precession timescale, to characterize the orbit: (J, ξ).

Figure 5 shows posterior probability distributions for $\Delta\Phi$, for several fiducial source events; Figure 7 shows corresponding posterior distributions for (J, ξ). To guide the eye, in Figure 7, a thick black line shows the allowed region for J, ξ assuming all mass and spin parameters are equal to the source parameters, as in Figure 3. First and foremost, as noted above, the measurements shown in Figure 5 immediately reveal that $\Delta\Phi$ at $f = 100$Hz can be measured for many binaries which do not have $\mathbf{S}_{1,2}$ parallel to $\mathbf{L}$. Though nominally an intrinsic parameter tied to the phase of the spins' relative precession cycle, the parameter $\Delta\Phi$ is limited by the range of precession dynamics allowed by the system at f_{ref}. Second, the posterior in (J, ξ) is highly nongaussian, as shown in Figure 7. Finally, precession-induced modulation is known to break all degeneracies and enable strong constraints on many parameters [35, 37, 38, 41, 63–65]. As shown by the bottom panel of Figure 7, our ability to constrain the posterior distributions in (J, ξ) and in mass ratio is correlated.

Figure 8 shows the posterior distributions for sources with different orientation θ_{JN} relative to the line of sight. Similar to the change in morphology constraints with θ_{JN}, the extent of the posterior distribution in the $J\xi$-plane increases (roughly) as $\sin\theta_{JN}$. Nearly face-on sources have little precession-induced modulation in their GW signal, and therefore measurements cannot as reliably infer J, ξ.

Finally, Figure 9 shows the posterior distributions for sources with different network amplitudes (SNR). Similar to the change in morphology constraints with SNR, the extent of the posterior distribution in the $J\xi$-plane increases as the source SNR decreases.

Comparing our results to the prior J, ξ distribution shown in Figure 3 suggests the wide prior convention has a significant impact on the posterior distribution, "pulling" the posterior away from the region most strongly supported by the data. We anticipate that astrophysically motivated priors which favor larger spins and more comparable mass ratios should produce tighter constraints on J, ξ and morphology.

C. Natural timescales as coordinates for double-spin measurements

Rather than using the conserved constants (J, ξ) to characterize spin precession, we can use the two natural precession frequencies $(\langle\Omega_z/(2\pi)\rangle, 1/\tau)$ introduced in [22, 23] and reviewed in Appendix B. Unlike the instantaneous precession vectors which appear in $d\mathbf{S}_{1,2}/dt$, these expressions are independent of precession phase.

Moreover, even for high-symmetry configurations like nearly aligned spins and post-Newtonian resonances, these timescales – corresponding to the *rate* of precessional modulation – are except for one special case well-defined and finite,[6] though the associated *amplitudes* can be zero. For example, the frequency $\langle\Omega_z\rangle \equiv \alpha/\tau$ is nonzero for binaries with $\mathbf{L}, \mathbf{S_1}, \mathbf{S_2}$ all parallel, as can most easily be demonstrated in the special case of a single precessing spin [18]. Similarly, even though no modulation on the timescale takes place in post-Newtonian resonances, where spins and $\mathbf{L}$ remain coplanar, the spin precession timescale τ is well-defined and nonzero [23].

As described in Appendix B, due to coordinate ambiguity when $\mathbf{J}$ and $\mathbf{L}$ are parallel, the angle α can change by 2π on two distinct surfaces in the $J\xi$-plane, but is otherwise continuous. The function τ is continuous. Because the coordinate transformation from (J, ξ) to $(\langle\Omega_z\rangle/(2\pi), 1/\tau)$ has two simple discontinuities, the connected posterior distributions in (J, ξ) seen above can map to two regions in $(\langle\Omega_z\rangle/(2\pi), 1/\tau)$ when the posterior distribution is sufficiently poorly constrained or close to these critical surfaces. More broadly, the transformation between J, ξ and Ω_z, τ may not always be globally one-to-one: the transformation might lose some information. That said, because these timescales occur in the dynamics and hence waveform, their imprint should appear in the posterior distribution, as with single-spin binaries [38].

Figure 10 shows the posterior in these "observable" parameters: the precession frequencies $\langle\Omega_z\rangle$ and $1/\tau$, evaluated at a GW frequency of 100Hz. First and foremost, except for outliers associated with nearly aligned sources and templates, this figure suggests that, as a first approximation, GW measurements isolate a candidate source to a relatively narrow region of the $(\langle\Omega_z\rangle, 1/\tau)$ plane. These tight limits are only possible with sufficient leverage to identify both timescales in the modulated signal: when the viewing angle is small ($\theta_{JN} \simeq 0$) or precession-induced modulation is small ($\hat{\mathbf{L}} \cdot \hat{\mathbf{J}} \simeq 1$, as with $\Delta\Phi = \pi$; see Figure 2), then observations cannot pin down both timescales. Second, because $\langle\Omega_z\rangle = \alpha/\tau$ is not a continuous function of (J, ξ), due to ambiguity in defining the precession angle α for some degenerate geometries, a posterior that is connected in the $J\xi$-plane can be disconnected in the $(\langle\Omega_z\rangle, \tau)$ plane. That said, particularly for the narrowly confined $\Delta\Phi = 0$ sources, the posterior in Ω_z is connected. Third, for spin-orbit resonances, no relative spin precession occurs – all spins remain coplanar – so no modulation on the timescale τ exists in the source spin dynamics; hence for all θ_{JN}, no modulations on the timescale τ can occur in the source

---

[6] As described in Gerosa *et al.* [61], for certain seperations a binary with both spins parallel to $\mathbf{L}$, with the more massive "up" and the less massive "down", is unstable to spin precession. When the instability occurs, a single point in the interior of the J, ξ region has $\tau = \infty$.
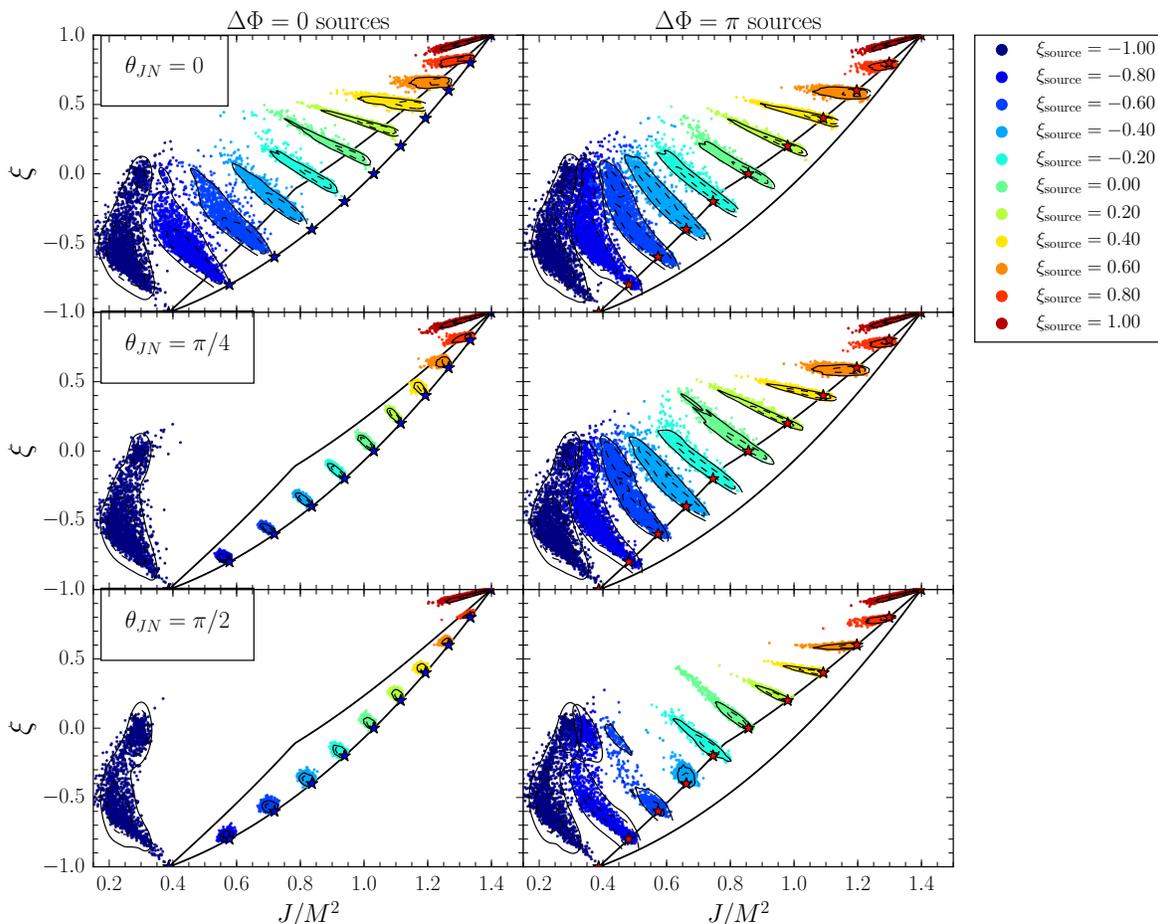
FIG. 8. **Constraining (J, ξ): dependence on θ_{JN}.** Posteriors from different simulations in the J, ξ plane for fixed SNR and different θ_{JN}, increasing from top ($\theta_{JN} = 0$) to bottom ($\theta_{JN} = \pi/2$). Points are colored according to the ξ values of the simulations; in this figure, all sources have SNR=20.

waveform. We hypothesize that this lack of modulation, unique to our choice of sources, contributes to the relative width of the posterior distributions in $1/\tau$ and $\langle \Omega_z \rangle$, though we cannot verify our hypothesis with this sample. Extrapolating from our sample, we further anticipate that sources with precession timescales τ comparable to or longer than the observationally accessible signal duration T_{wave} also cannot easily be distinguished from one another. Based on the limited sample available in our investigation, coordinates that are constant on the precession timescale like (J, ξ) and $(\langle \Omega_z \rangle, 1/\tau)$ are particularly valuable tools to extract robust statements about precessing binaries, isolating naturally correlated and tightly constrained parameters. Our methods generalize prior work using seperation-of-timescales to identify natural parameters and timescales for precessing black hole-neutron star binaries, and to relate those timescales to gravitational wave parameter estimation [18, 31, 38]. We anticipate these representations will be helpful when mining GW data from precessing BBHs for robust astrophysical statements.

D. Biases, the maximum likelihood estimate, and results with noise

Our study used doubly special sources. On the one hand, resonant binaries lie in a relatively small corner of the compact binary parameter space [22, 23]. On the other hand, the detector data we used was not a generic noise realization: for simplicity, we used exactly zero noise. As a result, as with posterior distributions of black hole spin and mass ratio for comparable-mass and highly spinning black holes, we generally cannot expect and do not observe the posterior confidence intervals in (J, ξ) or (Ω_z, τ) to be centered on the known source parameters: see e.g. Figs. 7 and 10. Though our posterior distributions had little support for the input binary's true parameters, our results are nonetheless well-converged and consistent with a single-best-fitting set of parameters close to the injected value. Figures 7 and 10 both show a cross ($\times$) at the location of the single sample with the maximum likelihood. Unlike the mean posterior value, our maximum likelihood estimates are generally much closer
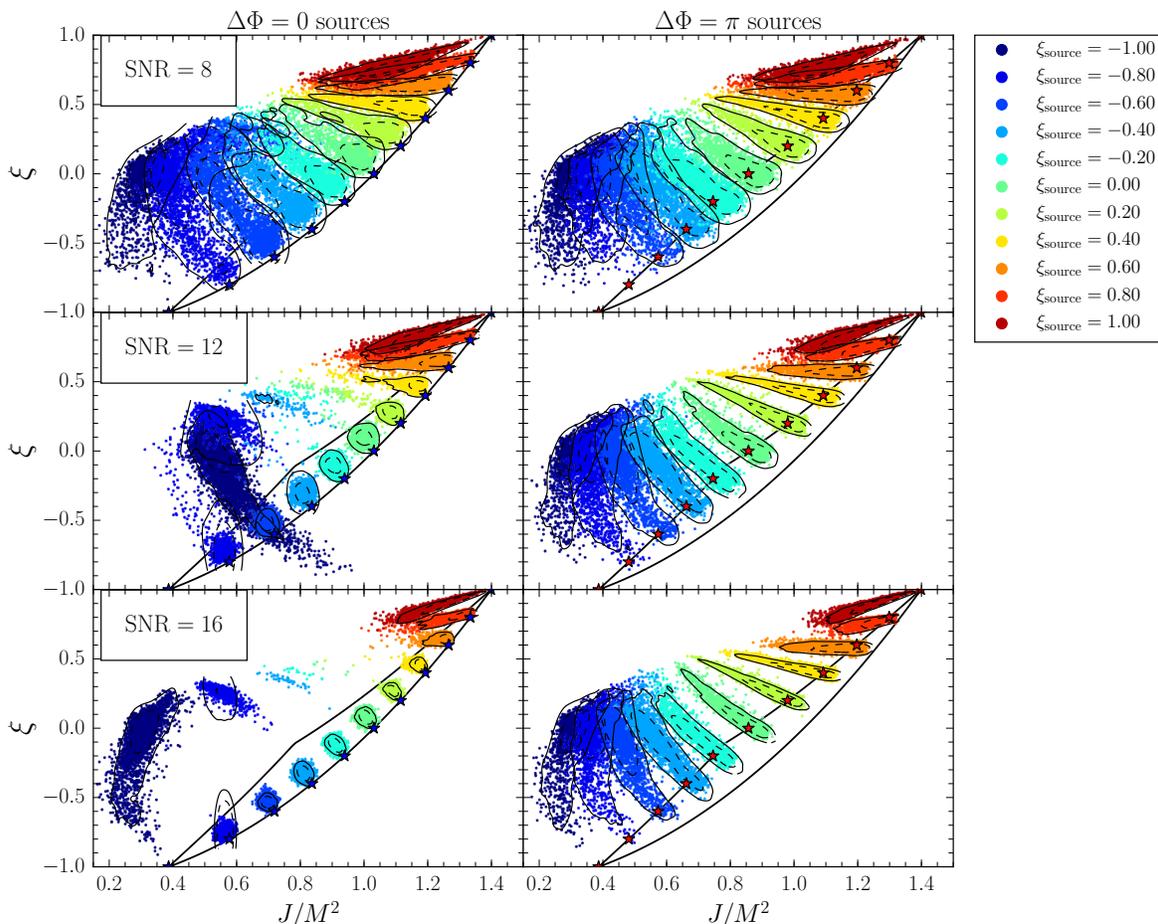
FIG. 9. **Constraining (J, ξ): dependence on SNR.** Posteriors from different simulations in the $J\xi$-plane for fixed $\theta_{JN} = \pi/4$ and different SNR, increasing from top (SNR = 8) to bottom (SNR = 16). Points are colored according to the simulation's ξ value.

to the injected value. Given how few posterior samples are available per run, we anticipate that observed differences between the maximum-likelihood estimates and the injected value are consistent with the limits of our finite sample size.

Owing to our exceptional inputs and unusual posteriors, to further demonstrate the stability of our results we repeated some of our analysis with a random noise realization. Figure 11 shows our results. The posterior distributions remain highly nongaussian, with structures similar to those observed in the zero-noise study.

E. Morphological classification: Data versus prior

Unlike conclusions derived about the chirp masses and spins [41–48], for properties that may be difficult to measure (such as the source morphology) the prior plays a surprisingly significant role. To quantify how much information we learn from the data, we compute the information gain (in bits) as the Kullback-Leibler (KL) divergence [66] between the morphological classification posterior and prior distributions:

$$D_{KL}(p||p_{\text{prior}}|\boldsymbol{\theta}) = \sum_i p(\mathcal{H}_i|\boldsymbol{\theta}) \log_2 \left(\frac{p(\mathcal{H}_i|\boldsymbol{\theta})}{p_{\text{prior}}(\mathcal{H}_i|\boldsymbol{\theta})} \right),$$

(7)

where $\boldsymbol{\theta} = \{\Delta\Phi, \xi, \theta_{JN}, \text{SNR}\}$. The KL divergence has seen increasing application in physics [67–70]. If the posterior resembles the prior ($p \sim p_{\text{prior}}$), we have learned nothing from the data and the KL divergence is nearly 0. To provide a sense of scale, for continuous gaussian distributions with the same mean but different standard deviations $\sigma \neq \sigma_*$, the KL divergence between these distributions is $D_{KL} \simeq [\ln(\sigma/\sigma_*)]^2/\ln 2$; a KL divergence of order unity therefore implies a difference in mean by one standard deviation, or a difference in variance by a factor of order 2. Figure 12 shows this information gain as a function of the source parameters $\Delta\Phi, \xi, \theta_{JN}$.

A comparison with Figure 4 reveals that, despite low posterior probabilities for $\Delta\Phi = \pi$ sources, even in the best case ($\theta_{JN} = \pi/2$) the peak amount of information we learn from the data is similar for the two source morphologies. The posterior probability depends signif-
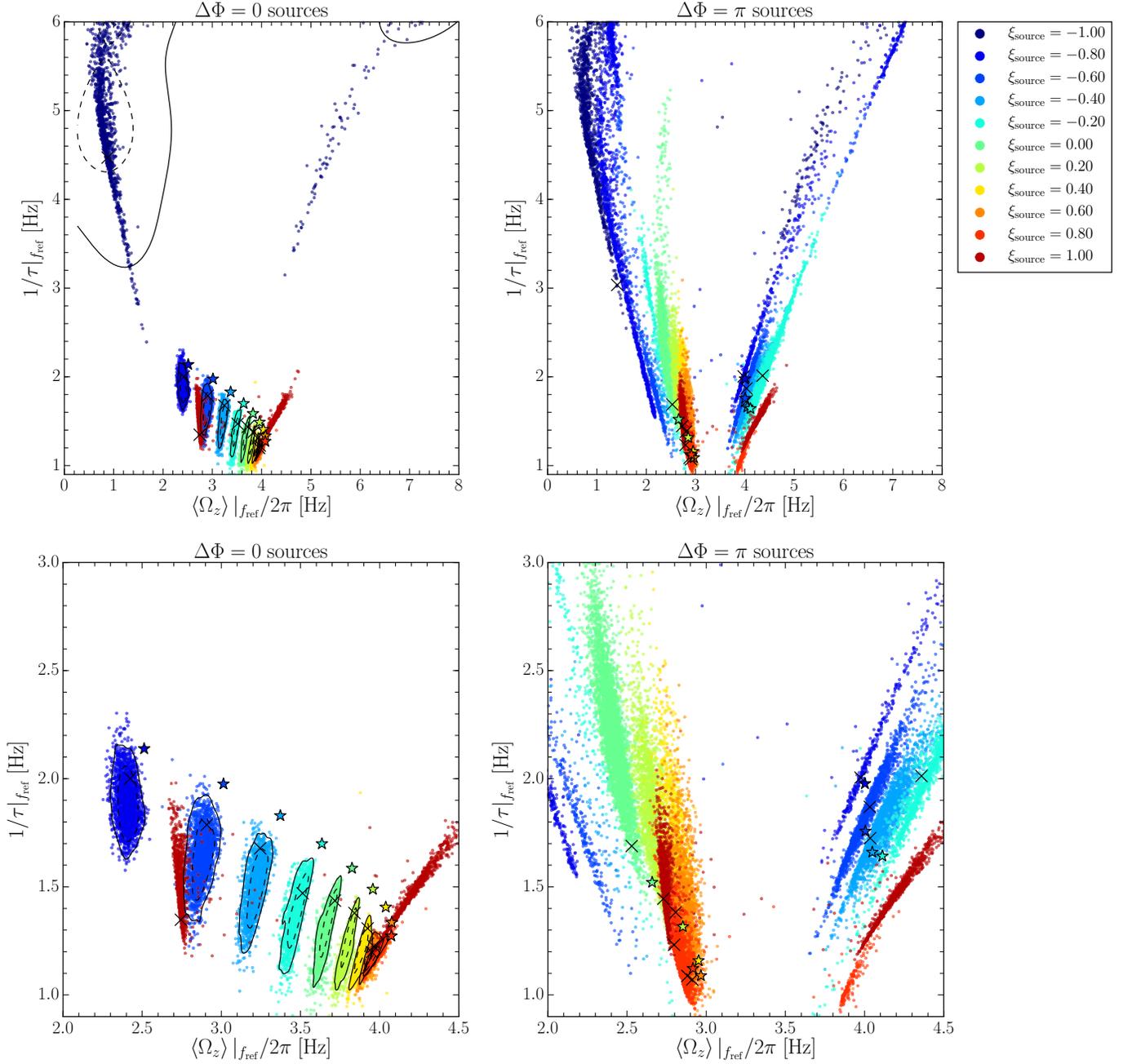
FIG. 10. **Constraining $(\langle\Omega_z\rangle, \tau)$ at 100 Hz.** Posterior distributions for the $\Delta\Phi = 0$ sources (top left) and $\Delta\Phi = \pi$ sources (top right) in the $(\langle\Omega_z\rangle/(2\pi), 1/\tau)$ plane, colored according to simulation ξ value. Values of τ and $\langle\Omega_z\rangle$ are evaluated using the binary configuration at the reference frequency $f_{\text{ref}} = 100$ Hz. Solid (dashed) lines show 95% (67%) confidence intervals for each set of posterior samples from distinct simulations. Points are colored according to the ξ values of the simulations which are marked by stars. Black crosses show, for each set of posterior samples, the maximum likelihood estimate. With few exceptions, the posterior associated with each $\Delta\Phi = 0$ injection is concentrated in a small range of $\langle\Omega_z\rangle$ and $1/\tau$ near the actual value. The results shown here are for $\theta_{JN} = \pi/2$, but similar results hold for $\theta_{JN} \geq \pi/4$. *Bottom*: Detail of the $\langle\Omega_z\rangle/(2\pi), 1/\tau$ plane, showing posteriors for simulations with $\xi \geq -0.4$.
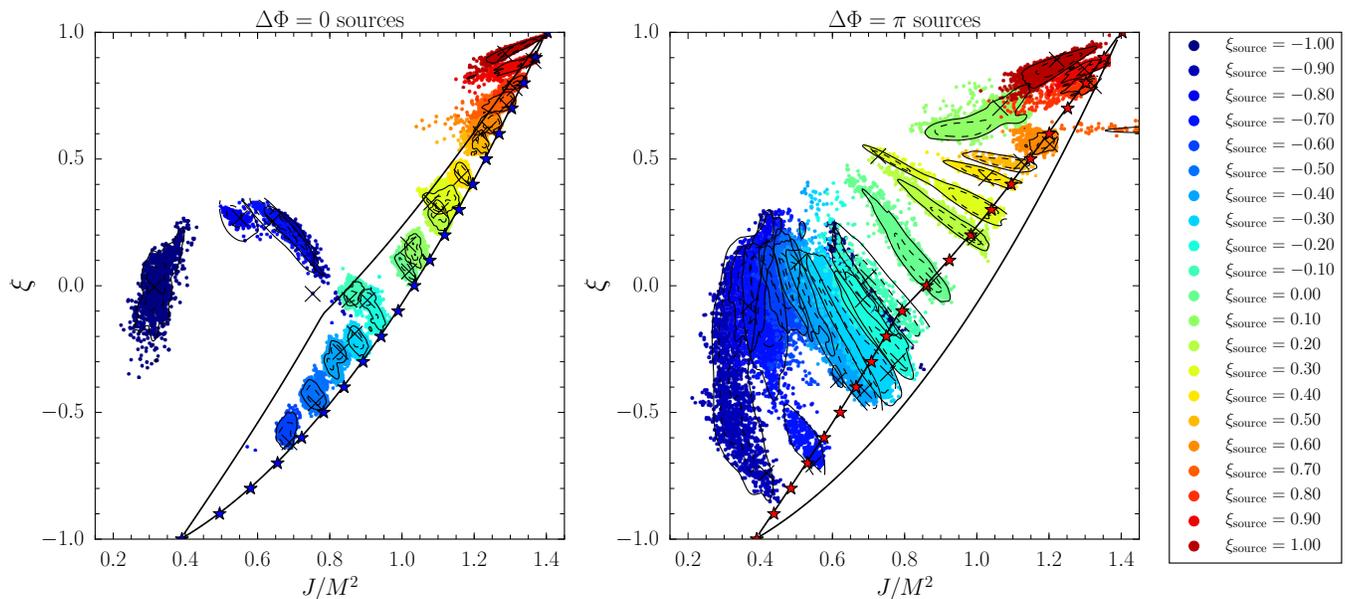
FIG. 11. **Effect of noise on the posterior.** As Figure 8, this figure shows the marginal posterior distribution in J, ξ for sources with $\theta_{JN} = \pi/4$ and SNR=20, but including a random noise realization. Stars mark the actual values of J and ξ from the simulations. Points and stars are and are colored according to the simulation's ξ value.

icantly on the prior. Specifically, even though the data often strongly favors $\mathcal{H}_\pi$, the relative rarity of $\mathcal{H}_\pi$ [Eq. (6)] is responsible for the relatively poor classifications for $\Delta\Phi = \pi$ sources, compared to $\Delta\Phi = 0$ sources. If we had adopted an astrophysically motivated prior, for example favoring comparable-mass binaries, we would have found a far more favorable result for the ability of GW measurements to distinguish between sources in distinct morphologies. We will address the impact of alternative priors in a subsequent study.

F. Systematic uncertainty and conservation of ξ

The quantity ξ is known to be conserved at 2PN order by the spin precession equations when the QM term [57] is included. This quantity may not be conserved at higher PN order, and it is known not to be conserved if the QM term is omitted. In this paper, we used the default model for black hole spin precession implemented in LALSIMULATION, which explicitly omitted the QM term. This omission was not intentional – indeed, all previous analyses also omitted this term [41–48] – but it provides an opportunity to assess the systematic error introduced when ξ is not exactly conserved on the spin precession timescale, as could occur at higher PN order.

Using the precession equations adopted in this analysis [18, 20],

$$\frac{d(\xi L M^2)}{dt} = -\frac{3\mathbf{L} \cdot \mathbf{S}_1 \times \mathbf{S}_2 v^7}{2\eta} \hat{\mathbf{L}} \cdot [\mathbf{S}_1(1+q) - \mathbf{S}_2(1+1/q)].$$

(8)

For configurations at or near a post-Newtonian resonance, ξ will remain nearly constant, because $\mathbf{L}, \mathbf{S}_1$ and $\mathbf{S}_2$ remain nearly coplanar.

For this reason, even though the PN spin precession equations do not enforce it, for all source binaries ξ is nearly constant throughout the evolution, rarely varying by as much as 0.05. Compared to the typical statistical measurement errors shown in Figures 7, 8 and 9, this systematic uncertainty is small for the signal amplitudes used in this study. Using a statistically significant subsample from each posterior distribution, we have also manually verified that ξ is nearly conserved, occasionally oscillating but in all cases varying by much less than the statistical uncertainty in the posterior. Finally, we have repeated some of the simulations shown in Figure 7 with the QM term included and find quantitatively similar results; see Figure 13. At least for the resonant sources used in this work, posterior parameter distributions are not sensitive to the inclusion of the QM term.

IV. CONCLUSIONS

In this work, we use the LALINFERENCE parameter estimation code to infer the parameters of precessing BBHs from their GW signal. Contrary to some claims that the subdominant spin has little observationally accessible effect [40], we demonstrate by concrete example that the distinctive signature of uniquely two-spin physics can be inferred for the special but conservative set of sources we chose, featuring exactly resonant sources with mass ratio $q = 0.8$, $M_{\text{tot}} = 13.5 M_\odot$ and maximal spins Specifically,
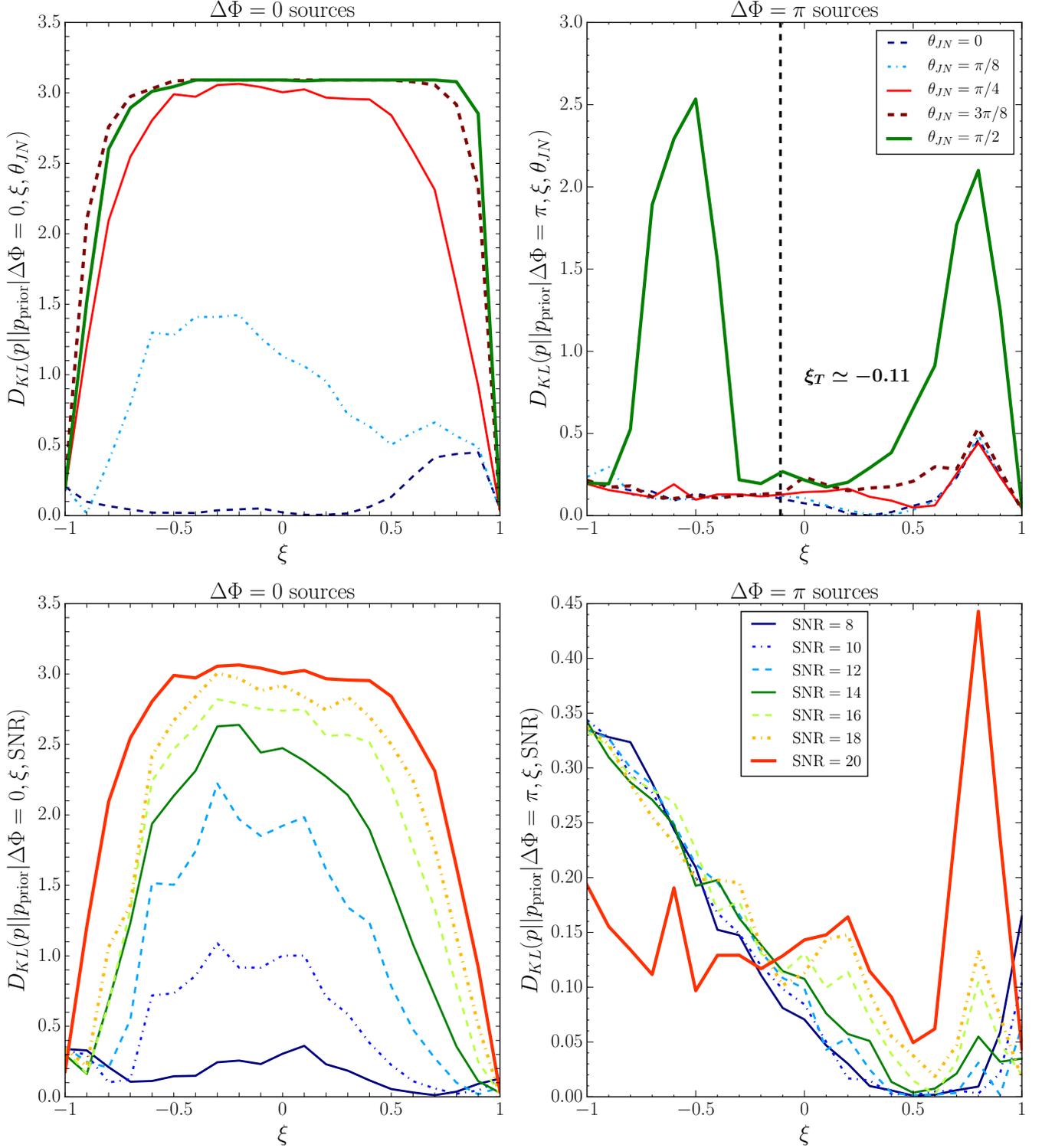
FIG. 12. **Information gain.** Kullback-Leibler (KL) divergence between the posterior and the prior distribution, measured in bits [Eq. (7)]. *Top:* KL divergence as a function of ξ and θ_{JN} for fixed SNR $= 20$. *Bottom:* KL divergence as a function of ξ and SNR for fixed $\theta_{JN} = \pi/4$. Structure in these plots reflects how the misalignment angles between the various angular momenta change versus ξ and how this affects information gain: cf. Figures 2 and 4. As described in Appendix C, the SNR=20 results (red curve) were produced using a lower starting frequency than results for SNR< 20; this discrepancy is responsible for the slight difference in trend between the bottom left panel's result for SNR=20 versus results for SNR< 20.
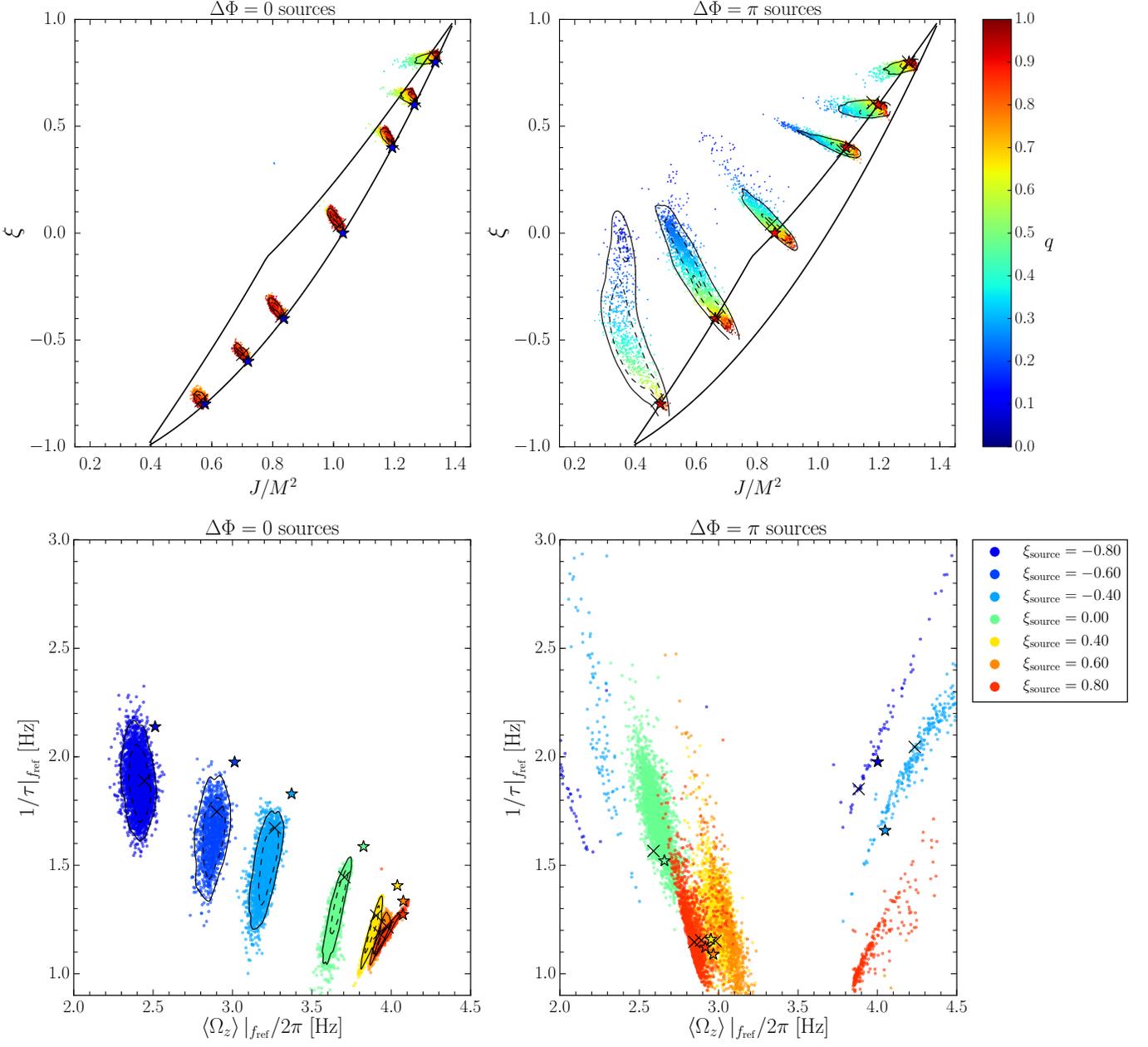
FIG. 13. **Results using QM-corrected spin precession**: After reproducing selected runs, we find similar posteriors in J, ξ (top panel; compare to Figure 7) and Ω_z, τ (bottom panel; compare to Figure 10, which adopts the same color scheme). Consistent with the corresponding figures, the top and bottom panel adopt different color schemes.

our analysis demonstrates that GW measurements can infer a subtle feature of the relative orientation of the two black hole spins: the binary's precessional morphology. Each posterior parameter distribution can be subdivided into three classes, identifying the relative probability that the progenitor binary had one of three characteristic behaviors (librating about $\Delta\Phi = 0$, librating about $\Delta\Phi = \pi$, or circulating). Using as sources the most extreme examples of the two librating cases – resonant binaries, which exhibit precession on only one of the two natural timescales – we confirmed the conclusion of [49] that resonant binaries can be correctly identified with the appropriate morphology. In other words, even though librating spins occupy a small part of parameter space, we show that these measurements reproducibly and correctly identify the neighborhood associated to each resonance, except for finely tuned highly symmetric configurations.

Because of computational cost our study focused on a single set of masses, spins. Further investigations with an astrophysically motivated distribution of masses, spins, and source distances are needed to assess how often and how reliably morphology can be classified in practice. Our promising (if preliminary) results support the hypothesis that morphological classification could be an astrophysically interesting and robust diagnostic, as distinct librating morphologies are both measurable and the natural consequence of distinct features of compact binary evolution [24].

Motivated by theoretical studies of precessing binaries [22, 23], we present our results in a new coordinate system ($\langle\Omega_z/(2\pi)\rangle, 1/\tau$), which better reflects the physical observables in the GW signal – precession-induced modulations in amplitude and phase – and respects precession physics, notably separation of timescales. Based on our limited study of special systems, this coordinate system seems to better characterize the dynamical information that GWs provide.

Recently, Ref. [40] used a small sample to investigate how well precessing BBH spins could be measured by Advanced LIGO-scale instruments, using a small number of mass combinations, spin orientations, and distances ($3 \times 2 \times 3$), but several viewing angles θ_{JN}. Like previous studies, the result of Vitale *et al.* [40] showed that posterior distributions depend sensitively on viewing angle, being best constrained when seen edge-on. Additionally, they investigated how well subdominant spins could be measured for precessing binaries, claiming on the basis of a limited sample that the relative angle $\Delta\Phi$ between the projection of the two spins into the orbital plane cannot be measured. Our results provide a concrete counterexample. That said, Ref. [40] used very different initial configurations with no resonant sources; they adopted suboptimal diagnostics for the second spin's orientation (i.e., the time-dependent azimuthal angle $\Delta\Phi$, like Fig. 5, instead of morphology as in Fig. 4 or J, ξ point as in Fig. 7); and they had too few independent initial conditions to robustly explore the full parameter space. Specifically, their sample included a handful of sources: three mass pairs, only one of which involved unequal-mass BH-BH binaries ($10M_\odot + 5M_\odot$); fixed BH spin magnitudes; and only two relative spin orientations, only one of which was not in $\mathcal{H}_C$ (i.e., not circulating). For their single noncirculating source – a ($10M_\odot, 5M_\odot$) pair of rapidly ($\chi_1 = \chi_2 = 0.9$) spinning black holes with initial spins $\mathbf{S_1}$ oriented by $45°$ and $\mathbf{S_2}$ oriented by $135°$ from the line of sight and coplanar with $\mathbf{L}$ – these authors do note that for $\theta_{JN} \simeq \pi/2$ the posterior distribution of $\Delta\Phi$ is significantly different from the prior. As noted above, further study with an astrophysically motivated distribution of masses, spins, source distances, and orientations is required to assess how well GWs can identify the source morphology of generic nonresonant sources.

Our analysis employed inspiral-only waveforms which lack the coalescence and ringdown signals present in real BBH merger signals. Their unphysical termination conditions are known to introduce convention-dependent artifacts into parameter estimation, with increasing impact as the total binary mass increases [71, 72]. A detailed discussion of waveform termination conditions is beyond the scope of this paper. That said, based on the relatively high termination frequencies shown in Table II, we anticipate that waveform termination conditions do not dominate the differences we observe.

Appendix A: Coordinate conventions for precessing spins

For reference and clarity, in this appendix we summarize the different coordinate conventions used to describe precessing spins: the radiation frame, in which angular momenta are parametrized relative to the line of sight; the "system frame" [39, 48], in which angular momenta are parametrized relative to the total angular momentum $\mathbf{J}$; the spin parameters $(\theta_{LS_1}, \theta_{LS_2}, \Delta\Phi)$ frequently used in the resonant-locking literature, in which the *spin* angular momenta are parametrized relative to the *orbital* angular momentum $\mathbf{L}$; and the (J, ξ, S) and (J, ξ, φ') coordinate sytems introduced in previous work [22, 23]. Unless otherwise noted, all parameters are specified at $f_{\rm ref} = 100$ Hz.

The radiation frame [20] expresses the orbital and spin angular momenta in polar coordinates relative to the direction of GW propagation $-\hat{\mathbf{N}}$, with the zero of azimuthal angle set by the plane spanned by $\mathbf{L}, -\hat{\mathbf{N}}$.

In the system frame [39], the angular momenta of the binary are characterized in a hierarchical fashion. The angles θ_{JN} and $\psi_{\rm J}$ are polar coordinates of the total angular momentum $\mathbf{J}$ direction relative to the direction of propagation $-\hat{\mathbf{N}}$; one angle ϕ_{JL} characterizes the relative orientation of $\mathbf{L}$ on its precession cone around the total angular momentum, equivalently constraining the direction of the total spin $\mathbf{S} = \mathbf{S}_1 + \mathbf{S}_2$; and three angles (t_1, t_2, ϕ_{12}) characterize the relative orientation of the two component spins relative to the orbital angular momentum. For example, $t_1 = \cos^{-1}\hat{\mathbf{S}}_1 \cdot \hat{\mathbf{L}}$ and, if $\hat{\mathbf{x}}$ and $\hat{\mathbf{y}}$ are unit vectors that form a right-handed orthonormal frame with $\hat{L}$, $e^{i\phi_{12}} = \mathcal{A} \times [(\hat{\mathbf{x}} + i\hat{\mathbf{y}}) \cdot \hat{\mathbf{S}}_2]/[(\hat{\mathbf{x}} + i\hat{\mathbf{y}}) \cdot \hat{\mathbf{S}}_1]$ where $\mathcal{A}$ is a real amplitude chosen so the norm of the right side is unity.

The resonant-locking literature uses parameters $\theta_1, \theta_2, \Delta\Phi$ to characterize the relative orientation of the two spins relative to $\mathbf{L}$. These parameters are identical to the tilt and relative phase angles ($t_1 = \theta_1 = \theta_{LS_1}$, $t_2 = \theta_2 = \theta_{LS_2}$, and $\Delta\Phi = \phi_{12}$) used in the system frame currently favored for LALINFERENCE [39].

Finally, recent work [22, 23] provides an explicit solution for the relative two-spin dynamics, expressing spin evolution in the three-dimensional relative spin space (e.g., $\theta_{LS_1}, \theta_{LS_2}, \Delta\Phi$) in yet another triplet of coordinates J, ξ, S on the three-dimensional space of all relative spin orientations at fixed L, S_1, S_2, and q. Gerosa *et al.* [23] also introduce an alternative coordinate system J, ξ, φ'. In these two systems, the first coordinate, the magnitude J of the total angular momentum, is a conserved constant on precession timescales; the projected effective spin ξ [cf. Eq. (2)] is conserved on all timescales by the orbit-averaged 2PN spin precession equations[7]; the coordinate S is the magnitude of the total spin; and the coordinate φ' is an angle characterizing the degree to which the plane spanned by $\mathbf{S}_1, \mathbf{S}_2$ is rotated relative to the plane spanned by $\mathbf{S}, \mathbf{L}$. Specifically, the angle φ' is defined by decomposing the spins relative to $\mathbf{S} = \mathbf{S_1} + \mathbf{S_2}$; a vector perpendicular to $\mathbf{S}, \mathbf{L}$; and the remaining vector of an orthonormal triad [Fig. 1 in [23]]:

$$\hat{\mathbf{Z}} \equiv \hat{\mathbf{S}}, \qquad \hat{\mathbf{Y}} \equiv \frac{\mathbf{L} \times \mathbf{S}}{|\mathbf{L} \times \mathbf{S}|}, \qquad \hat{\mathbf{X}} = \hat{\mathbf{Y}} \times \hat{\mathbf{Z}}. \quad \text{(A1)}$$

In terms of these coordinates, we can redundantly express the spin using the spin magnitude S and the relative angle φ' between the plane spanned by the two spins and the plane spanned by $\mathbf{S}$ and $\mathbf{L}$:

$$\mathbf{S}_1 = \mathcal{A}\mathbf{S} + b(\cos\varphi'\hat{\mathbf{X}} + \sin\varphi'\hat{\mathbf{Y}}) \qquad \text{(A2a)}$$

$$\mathbf{S}_2 = (1 - \mathcal{A})\mathbf{S} - b(\cos\varphi'\hat{\mathbf{X}} + \sin\varphi'\hat{\mathbf{Y}}) \qquad \text{(A2b)}$$

$$\mathcal{A} = \frac{S^2 + S_1^2 - S_2^2}{2S^2}; \qquad 1 - \mathcal{A} = \frac{S^2 + S_2^2 - S_1^2}{2S^2} \quad \text{(A2c)}$$

$$b^2 = S_1^2 - \mathcal{A}^2 S^2 \qquad \text{(A2d)}$$

Either the phase angle φ' or the spin S can be eliminated from these expressions; see Gerosa *et al.* [23] for details.

Appendix B: Spin precession formulae

For each value of $m_1, m_2, \chi_1, \chi_2, L, J, \xi$, Refs. [22, 23] define two quantities that characterize precession: α and τ. The timescale τ is the duration of one precession cycle of the spins relative to $\mathbf{L}$, defined by

$$\tau = 2 \int_{S_-}^{S_+} \frac{dS}{|dS/dt|} \qquad \text{(B1)}$$

where S is the magnitude of the total spin (cf. Appendix A) and where $(dS/dt)^2$ is a polynomial in S with simple roots at the turning points $S = S_\pm$. Because $1/|dS/dt|$ has an integrable singularity at both limits $S_\pm$, τ is finite and continuous everywhere, except under certain conditions at the single point in the (J, ξ) plane associated with the larger spin aligned and the smaller spin antialigned with $\mathbf{L}$ [61]. By contrast, the angle α is the azimuthal angle accumulated during the precession of $\mathbf{L}$ around $\mathbf{J}$. The azimuthal angle ϕ_{JL} of $\mathbf{L}$ around $\mathbf{J}$ is is therefore not well defined at times when $\mathbf{L}$ and $\mathbf{J}$ are parallel. As an integral of $d\phi_{JL}/dt$, α inherits this ambiguity. Away from this surface, the function α is well-defined, continuous, and can be evaluated using the definite integral

$$\alpha \equiv 2 \int_{S_-}^{S_+} \Omega_z \frac{dS}{|dS/dt|} \qquad \text{(B2)}$$

—————

[7] Using the complete 2PN spin precession equations, without orbit averaging, ξ varies on the orbital timescale.

where the rational function Ω_z is given by Eq. (19) in [22]. This discontinuity in α arises from an integrable singularity in Ω_z; it implies a discontinuity in α/τ, and it is responsible for the V-shapes seen in Figure 10.

Because the $J\xi$-plane and $\langle\Omega_z\rangle = \alpha/\tau$ play a significant role in our presentation, we provide an explicit formula to determine where these discontinuities occur. The conditions on (J, ξ) needed for colinearity follow from Eqs. (6) and (14) in [23], after substituting suitable values of S. For clarity, we also derive them from straightforward vector algebra. Because colinearity of $\mathbf{L}$ and $\mathbf{J}$ implies all angular momenta are coplanar, without loss of generality we use the polar angles $\theta_{JS_1}, \theta_{JS_2} \in [0, \pi]$ of $\mathbf{S}_{1,2}$ relative to $\mathbf{J}$ to characterize the two spins. In these coordinates, colinearity of $\mathbf{L}$ and $\mathbf{J}$ requires

$$J = sL + S_1 \cos\theta_{JS_1} + S_2 \cos\theta_{JS_2} \tag{B3}$$

$$0 = S_1 \sin\theta_{JS_1} + S_2 \sin\theta_{JS_2} \tag{B4}$$

$$\xi = \frac{s}{M}[m_1\chi_1 \cos\theta_{JS_1} + m_2\chi_2 \cos\theta_{JS_2}] \tag{B5}$$

where $s = \pm 1$ corresponds to two possible choices (alignment or antialignment) between the orbital and total angular momentum: $\hat{\mathbf{J}} = s\hat{\mathbf{L}}$

Keeping in mind that $\theta_{JS_1}, \theta_{JS_2} \in [0, \pi]$, we find without loss of generality that these conditions imply one quadratic equation and one system of two linear equations on the variables $\cos\theta_{JS_1}, \cos\theta_{JS_2}$:

$$S_1^2(1 - \cos^2\theta_{JS_1}^2) = S_2^2(1 - \cos\theta_{JS_2}^2) \tag{B6}$$

$$\begin{bmatrix} J - sL \\ s\xi \end{bmatrix} = \begin{bmatrix} m_1^2 & m_2^2 \\ m_1/M & m_2/M \end{bmatrix} \begin{bmatrix} \chi_1 \cos\theta_{JS_1} \\ \chi_2 \cos\theta_{JS_2} \end{bmatrix} \tag{B7}$$

Solving the linear equations for $\cos\theta_{JS_1}, \cos\theta_{JS_2}$ and then substituting into the quadratic constraint generally leads to a quadratic form in (J, ξ). For this problem, however, the coefficient of ξ^2 cancels, leaving a *linear* expression for ξ as a function of J. The solution [compare e.g. to Eq. (13) in [23]] reads

$$\xi = s\frac{(J - Ls)^2 - \frac{(m_1 - m_2)}{m_1 + m_2}(S_1^2 - S_2^2)}{2\eta M^2(J - Ls)}$$

$$= s\frac{(1 + q)^2(J - Ls)^2 - (1 - q^2)(S_1^2 - S_2^2)}{2q(J - Ls)M^2}. \tag{B8}$$

Using this solution, we find that the angles $\theta_{JS_1}, \theta_{JS_2}$ vary with J according to

$$\cos\theta_{JS_1} = \frac{[(J - Ls)^2 + (S_1^2 - S_2^2)]}{2S_1(J - Ls)}, \tag{B9}$$

$$\cos\theta_{JS_2} = \frac{[(J - Ls)^2 - (S_1^2 - S_2^2)]}{2S_2(J - Ls)}. \tag{B10}$$

Not all values of J correspond to realizable angles for $\theta_{JS_1}, \theta_{JS_2}$. For geometric reasons – and as can be immediately verified by direct substitution of appropriate choices for J, namely $J = L \pm S_1 \pm S_2$ – the curve with $s = 1$ passes through all four aligned-spin configurations
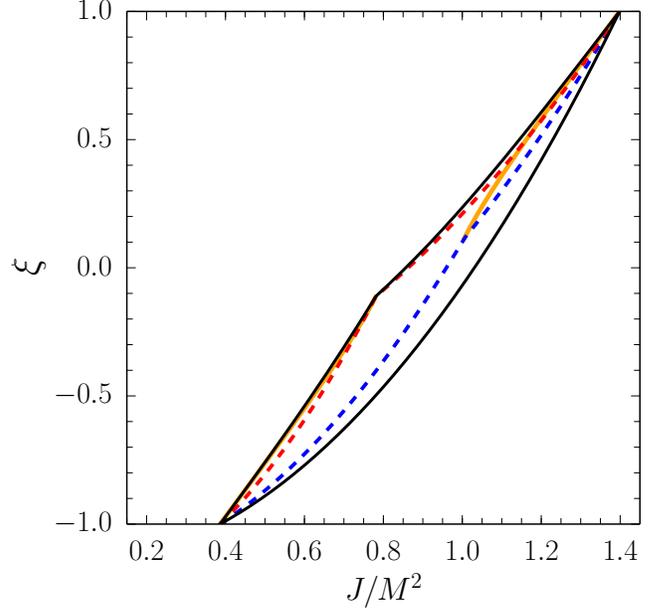
FIG. 14. **Alignment between L and J and discontinuities in α in the $J\xi$-plane.** As in Figure 3, the thick black lines show the allowed region in the $J\xi$-plane for our fiducial parameters, and the dashed lines show $J_{c0,c\pi}(\xi)$. The orange curves show the locus of points J, ξ where $\mathbf{L}$ and $\mathbf{J}$ are parallel and thus where α is discontinuous, as determined by solutions to Eq. (B8) that correspond to physically realizable spin orientations.

$|\cos\theta_{JS_1}| = |\cos\theta_{JS_2}| = 1$. Conversely, for $s = 1$, a region containing $J = L$ is always excluded. In the language of [23], the root $s = 1$ corresponds to $S_{\min} = |J - L|$ and the root $s = -1$ corresponds to $S_{\max} = J + L$. For example, as illustrated by Figure 14 for our fiducial parameters, one of these curves (orange in the figure) connects the point $\cos\theta_{JS_1} = \cos\theta_{JS_2} = 1$ to the "kink" in the $J_{c0}(\xi)$ curve corresponding to $\theta_{JS_1} = \pi, \theta_{JS_2} = 0$, the "up/down" instability point where $\tau = \infty$ [61]. The other curve joins the remaining two spin-aligned configurations and is nearly equal to the minimum value $J_{\min}(\xi)$ allowed at each ξ over the corresponding range of ξ. This latter discontinuity is responsible for the significant change in Ω_z at $\xi = \xi_T$ seen in Table II, and for the V-shape feature seen in Figure 10.

Appendix C: Technical details and caveats

Small technical details about waveform generation and sampling can have a dramatic impact on final results. In this appendix, we provide more exhaustive details about the specific calculations we perform.

All signals are sampled with an interval $\Delta t = 1/2048$s, corresponding to a Nyquist frequency $f_{\text{Nyq}} = 1024$Hz. Our signal and templates start at $2f_{\text{orb}} = 10$Hz. [For sources with SNR < 20, we used $2f_{\text{orb}} = 20$Hz.] Each bi-

$\Delta\Phi$	ξ	J/M^2	$f_{\rm end}$(Hz)	$\Delta\phi_{JL}/2\pi$	θ_{JL}	θ_{LS_1}	θ_{LS_2}	$\langle\Omega_z\rangle/2\pi$[Hz]	$1/\tau$[Hz]
0	-1.0	0.39	281	3.50	0.00	π	π	-	-
0	-0.9	0.49	303	3.98	0.46	2.63	2.79	2.13	2.16
0	-0.8	0.58	321	4.47	0.55	2.41	2.63	2.46	2.07
0	-0.7	0.66	345	4.83	0.58	2.23	2.51	2.73	1.99
0	-0.6	0.72	375	5.20	0.59	2.09	2.39	2.95	1.92
0	-0.5	0.78	403	5.59	0.59	1.95	2.29	3.14	1.84
0	-0.4	0.84	438	5.94	0.58	1.83	2.19	3.30	1.77
0	-0.3	0.89	483	6.25	0.56	1.71	2.09	3.44	1.71
0	-0.2	0.94	533	6.58	0.55	1.60	1.99	3.55	1.65
0	-0.1	0.99	608	6.88	0.52	1.50	1.90	3.65	1.59
0	0.0	1.03	687	7.18	0.50	1.39	1.80	3.74	1.54
0	0.1	1.08	763	7.47	0.47	1.29	1.69	3.81	1.49
0	0.2	1.12	812	7.73	0.45	1.19	1.59	3.87	1.44
0	0.3	1.16	812	7.99	0.42	1.09	1.48	3.91	1.40
0	0.4	1.20	834	8.22	0.39	0.99	1.36	3.95	1.36
0	0.5	1.23	823	8.48	0.35	0.88	1.23	3.97	1.33
0	0.6	1.27	825	8.67	0.31	0.77	1.10	3.99	1.30
0	0.7	1.30	831	8.90	0.27	0.66	0.95	3.99	1.26
0	0.8	1.34	865	9.11	0.22	0.53	0.77	3.99	1.23
0	0.9	1.37	857	9.29	0.16	0.37	0.54	3.97	1.21
0	1.0	1.40	843	9.47	0.00	0.00	0.00	-	-
π	-1.0	0.39	281	6.29	0.00	π	π	-	-
π	-0.9	0.44	299	6.44	0.04	2.84	2.55	-	-
π	-0.8	0.48	317	6.62	0.06	2.74	2.27	3.92	1.92
π	-0.7	0.53	336	6.83	0.08	2.69	2.04	3.91	1.80
π	-0.6	0.58	359	7.05	0.09	2.67	1.81	3.92	1.71
π	-0.5	0.62	384	7.30	0.10	2.68	1.58	3.94	1.65
π	-0.4	0.67	413	7.57	0.10	2.72	1.33	3.96	1.61
π	-0.3	0.71	444	7.92	0.09	2.78	1.05	3.99	1.60
π	-0.2	0.75	481	8.29	0.07	2.89	0.71	4.02	1.60
π	-0.1	0.79	518	4.51	0.06	2.92	0.10	2.47	1.59
π	-0.0	0.86	569	4.80	0.16	2.43	0.32	2.60	1.48
π	0.1	0.92	636	5.12	0.19	2.14	0.44	2.71	1.38
π	0.2	0.98	712	5.44	0.20	1.91	0.53	2.79	1.28
π	0.3	1.04	755	5.72	0.19	1.69	0.60	2.85	1.20
π	0.4	1.10	799	5.96	0.17	1.49	0.65	2.89	1.13
π	0.5	1.15	819	6.23	0.15	1.30	0.67	2.91	1.08
π	0.6	1.20	834	6.46	0.13	1.11	0.66	2.90	1.06
π	0.7	1.25	850	6.65	0.10	0.92	0.62	2.89	1.07
π	0.8	1.30	864	6.80	0.08	0.72	0.53	2.86	1.09
π	0.9	1.35	879	6.91	0.05	0.49	0.39	2.82	1.13
π	1.0	1.40	843	6.98	0.00	0.00	0.00	-	-

TABLE II. **Derived source properties.** For each dynamically distinct binary used as a source of GWs, this table reports on properties of the dynamics, including: $f_{\rm end}$, the termination frequency of the GW signal; $\Delta\phi_{JL}$, the number of precession cycles of **L** around **J** between the starting and ending frequencies; $\theta_{JL}, \theta_{LS_1}, \theta_{LS_2}$, characterizing the relative orientations of the angular momenta $\mathbf{J}, \mathbf{L}, \mathbf{S_1}, \mathbf{S_2}$; J, the magnitude of the total angular momentum; and $\langle\Omega_z\rangle/(2\pi)$ and $1/\tau$, the characteristic precession frequencies. The last five columns are evaluated at the reference frequency, 100Hz. Discontinuities in $\langle\Omega_z\rangle$ occur as described in Appendix B.

nary is evolved until terminated at the minimum stable circular orbit or when the orbital frequency begins to decrease with time, whichever comes first. For the masses and spins studied here, this termination frequency is significantly smaller than the Nyquist frequency, but significantly higher than the frequency at which most power accumulates; see, e.g., Fig 4 in [49].

Our signals were analyzed in a 128s data window, far longer than the signal. [For sources with SNR < 20, we used 16s.] As described elsewhere, rather than use the full 15-dimensional likelihood, we explicitly marginalized

it over time and orbital phase at each step in the MCMC [48]. Using selected examples, we have confirmed that our results are unchanged if this marginalization is not used. As seen in Table II, particularly for $\xi \simeq -1$, some of our signals were short, being terminated at comparatively small frequencies due to the breakdown of the post-Newtonian expansion we employ to generate them. That said, not only is relatively little signal power associated with $f \gtrsim 300$Hz, but also no structure in the posterior correlates tightly with the termination frequencies listed in Table II. A detailed study of the impact of termination

conditions on precessing parameter estimation is beyond the scope of our work.

With the exception of Figure 11, in the text we use an exactly zero-noise realization. The likelihood of a given set of GW detector data depends on the detector noise in two ways [47, 48]: through the specific detector data being analyzed, and through the probability of any given noise realization. Each instrument's noise $n(t)$ is assumed to be stationary and gaussian Markov process, characterized by a noise power spectrum $\langle \tilde{n}(\omega')^* \tilde{n}(\omega) \rangle = S_h(\omega)\delta(\omega - \omega')/2$; using the noise

power spectrum, we can evaluate the probability of any noise realization $n(t)$. To synthesize a unique data set to be analyzed for each set of intrinsic parameters λ, we assume that the data $d(t)$ in each instrument – generally containing both signal and noise, or of the form $d(t) = h(t|\lambda) + n(t)$ for each instrument — is given exactly by $d(t) = h(t) = F_+ h_+(t|\lambda) + F_\times h_\times(t|\lambda)$, where $F_{+,\times}$ are the detector response functions and $h_{+,\times}(t|\lambda)$ are the two linear polarizations of of the GW. Just like evaluating a normal distribution at the mean, this arbitrary choice eliminates ambiguity in subsequent Bayesian calculations of the posterior distribution.

[1] J. Abadie *et al.*, Classical and Quantum Gravity **27**, 173001 (2010), arXiv:1003.2480 [astro-ph.HE].

[2] M. Dominik, K. Belczynski, C. Fryer, D. E. Holz, E. Berti, T. Bulik, I. Mandel, and R. O'Shaughnessy, Astrophys. J. **759**, 52 (2012), arXiv:1202.4901 [astro-ph.HE].

[3] M. Dominik, K. Belczynski, C. Fryer, D. E. Holz, E. Berti, T. Bulik, I. Mandel, and R. O'Shaughnessy, Astrophys. J. **779**, 72 (2013), arXiv:1308.1546 [astro-ph.HE].

[4] M. Dominik, E. Berti, R. O'Shaughnessy, I. Mandel, K. Belczynski, C. Fryer, D. E. Holz, T. Bulik, and F. Pannarale, Astrophys. J. **806**, 263 (2015), arXiv:1405.7016 [astro-ph.HE].

[5] The LIGO Scientific Collaboration, Classical and Quantum Gravity **32**, 074001 (2015).

[6] F Acernese *et al.*, Classical and Quantum Gravity **32**, 024001 (2015).

[7] C. S. Unnikrishnan, International Journal of Modern Physics D **22**, 1341010 (2013).

[8] K. Somiya, Classical and Quantum Gravity **29**, 124007 (2012), arXiv:1111.7185 [gr-qc].

[9] Y. Sakakibara, T. Akutsu, D. Chen, A. Khalaidovski, N. Kimura, S. Koike, T. Kume, K. Kuroda, T. Suzuki, C. Tokoku, and K. Yamamoto, Classical and Quantum Gravity **31**, 224003 (2014).

[10] M. Punturo *et al.*, Classical and Quantum Gravity **27**, 194002 (2010).

[11] P. C. Peters and J. Mathews, Physical Review **131**, 435 (1963).

[12] P. C. Peters, Physical Review **136**, 1224 (1964).

[13] U. Sperhake, E. Berti, V. Cardoso, J. A. González, B. Brügmann, and M. Ansorg, Phys. Rev. D **78**, 064069 (2008), arXiv:0710.3823 [gr-qc].

[14] I. Hinder, F. Herrmann, P. Laguna, and D. Shoemaker, Phys. Rev. D **82**, 024033 (2010), arXiv:0806.1037 [gr-qc].

[15] N. Yunes, K. G. Arun, E. Berti, and C. M. Will, Phys. Rev. D **80**, 084001 (2009), arXiv:0906.0313 [gr-qc].

[16] W. E. East, S. T. McWilliams, J. Levin, and F. Pretorius, Phys. Rev. D **87**, 043004 (2013), arXiv:1212.0837 [gr-qc].

[17] E. A. Huerta, P. Kumar, S. T. McWilliams, R. O'Shaughnessy, and N. Yunes, Phys. Rev. D **90**, 084016 (2014), arXiv:1408.3406 [gr-qc].

[18] T. A. Apostolatos, C. Cutler, G. J. Sussman, and K. S. Thorne, Phys. Rev. D **49**, 6274 (1994).

[19] L. E. Kidder, Phys. Rev. D **52**, 821 (1995), gr-qc/9506022.

[20] Y. Pan, A. Buonanno, Y. Chen, and M. Vallisneri, Phys. Rev. D **69**, 104017 (2004).

[21] J. D. Schnittman, Phys. Rev. D **70**, 124020 (2004), astro-ph/0409174.

[22] M. Kesden, D. Gerosa, R. O'Shaughnessy, E. Berti, and U. Sperhake, Physical Review Letters **114**, 081103 (2015), arXiv:1411.0674 [gr-qc].

[23] D. Gerosa, M. Kesden, U. Sperhake, E. Berti, and R. O'Shaughnessy, Phys. Rev. D **92**, 064016 (2015), arXiv:1506.03492 [gr-qc].

[24] D. Gerosa, M. Kesden, E. Berti, R. O'Shaughnessy, and U. Sperhake, Phys. Rev. D **87**, 104028 (2013), arXiv:1302.4442 [gr-qc].

[25] K. Belczynski, R. E. Taam, E. Rantsiou, and M. van der Sluys, Astrophys. J. **682**, 474 (2008), astro-ph/0703131.

[26] I. Mandel and R. O'Shaughnessy, Classical and Quantum Gravity **27**, 114007 (2010), arXiv:0912.1074 [astro-ph.HE].

[27] R. O'Shaughnessy, B. Farr, E. Ochsner, H.-S. Cho, V. Raymond, C. Kim, and C.-H. Lee, Phys. Rev. D **89**, 102005 (2014), arXiv:1403.0544 [gr-qc].

[28] S. Stevenson, F. Ohme, and S. Fairhurst, Astrophys. J. **810**, 58 (2015), arXiv:1504.07802 [astro-ph.HE].

[29] E. Ochsner and R. O'Shaughnessy, Phys. Rev. D **86**, 104037 (2012), arXiv:1205.2287 [gr-qc].

[30] R. O'Shaughnessy, L. London, J. Healy, and D. Shoemaker, Phys. Rev. D **87**, 044038 (2013), arXiv:1209.3712 [gr-qc].

[31] D. A. Brown, A. Lundgren, and R. O'Shaughnessy, Phys. Rev. D **86**, 064020 (2012), arXiv:1203.6060 [gr-qc].

[32] A. Lundgren and R. O'Shaughnessy, Phys. Rev. D **89**, 044021 (2014).

[33] A. Klein, N. Cornish, and N. Yunes, Phys. Rev. D **88**, 124015 (2013), arXiv:1305.1932 [gr-qc].

[34] A. H. Mroué *et al.*, Phys. Rev. Lett. **111**, 241104 (2013), arXiv:1304.6077 [gr-qc].

[35] M. V. van der Sluys, C. Röver, A. Stroeer, V. Raymond, I. Mandel, N. Christensen, V. Kalogera, R. Meyer, and A. Vecchio, ApJL **688**, L61 (2008), arXiv:0710.1897.

[36] M. van der Sluys, V. Raymond, I. Mandel, C. Röver, N. Christensen, V. Kalogera, R. Meyer, and A. Vecchio, Classical and Quantum Gravity **25**, 184011 (2008), arXiv:0805.1689 [gr-qc].

[37] H. Cho, E. Ochsner, R. O'Shaughnessy, C. Kim, and

C. Lee, Phys. Rev. D **87**, 02400 (2013), arXiv:1209.4494.

[38] R. O'Shaughnessy, B. Farr, E. Ochsner, H.-S. Cho, V. Raymond, C. Kim, and C.-H. Lee, Phys. Rev. D **89**, 102005 (2014).

[39] B. Farr, E. Ochsner, W. M. Farr, and R. O'Shaughnessy, Phys. Rev. D **90**, 024018 (2014), arXiv:1404.7070 [gr-qc].

[40] S. Vitale, R. Lynch, J. Veitch, V. Raymond, and R. Sturani, Physical Review Letters **112**, 251101 (2014), arXiv:1403.0129 [gr-qc].

[41] J. Aasi *et al.*, Phys. Rev. D **88**, 062001 (2013).

[42] W. Del Pozzo, J. Veitch, and A. Vecchio, Phys. Rev. D **83**, 082002 (2011), arXiv:1101.1391 [gr-qc].

[43] N. Cornish, L. Sampson, N. Yunes, and F. Pretorius, Phys. Rev. D **84**, 062003 (2011), arXiv:1105.2088 [gr-qc].

[44] T. G. F. Li, W. Del Pozzo, S. Vitale, C. Van Den Broeck, M. Agathos, J. Veitch, K. Grover, T. Sidery, R. Sturani, and A. Vecchio, Phys. Rev. D **85**, 082003 (2012), arXiv:1110.0530 [gr-qc].

[45] J. Veitch, I. Mandel, B. Aylott, B. Farr, V. Raymond, C. Rodriguez, M. van der Sluys, V. Kalogera, and A. Vecchio, Phys. Rev. D **85**, 104045 (2012), arXiv:1201.1195 [astro-ph.HE].

[46] S. Nissanke, J. Sievers, N. Dalal, and D. Holz, Astrophys. J. **739**, 99 (2011), arXiv:1105.3184 [astro-ph.CO].

[47] R. O'Shaughnessy, B. Farr, E. Ochsner, H.-S. Cho, C. Kim, and C.-H. Lee, Phys. Rev. D **89**, 064048 (2014), arXiv:1308.4704 [gr-qc].

[48] J. Veitch *et al.*, Phys. Rev. D **91**, 042003 (2015), arXiv:1409.7215 [gr-qc].

[49] D. Gerosa, R. O'Shaughnessy, M. Kesden, E. Berti, and U. Sperhake, Phys. Rev. D **89**, 124025 (2014), arXiv:1403.7147 [gr-qc].

[50] A. Gupta and A. Gopakumar, Classical and Quantum Gravity **31**, 105017 (2014), arXiv:1312.0217 [gr-qc].

[51] LIGO Algorithm Library, `https://www.lsc-group.phys.uwm.edu/daswg/projects/lal/nightly/docs/html/`.

[52] A. Buonanno, Y. Chen, and M. Vallisneri, Phys. Rev. D **67**, 104025 (2003), gr-qc/0211087.

[53] A. Buonanno, Y. Chen, Y. Pan, and M. Vallisneri, Phys. Rev. D **70**, 104003 (2004), gr-qc/0405090.

[54] A. Buonanno, B. R. Iyer, E. Ochsner, Y. Pan, and

B. S. Sathyaprakash, Phys. Rev. D **80**, 084043 (2009), arXiv:0907.0700 [gr-qc].

[55] C. M. Will and A. G. Wiseman, Phys. Rev. D **54**, 4813 (1996).

[56] T. Damour, Phys. Rev. D **64**, 124013 (2001), gr-qc/0103018.

[57] É. Racine, Phys. Rev. D **78**, 044021 (2008), arXiv:0803.1820 [gr-qc].

[58] LIGO Scientific Collaboration, `https://dcc.ligo.org/cgi-bin/DocDB/ShowDocument?docid=m060056`.

[59] J. Aasi *et al.*, ArXiv e-prints (2013), arXiv:1304.0670 [gr-qc].

[60] LIGO Scientific Collaboration, (2014), LIGO DCC T1400054, `https://dcc.ligo.org/LIGO-T1400054/public`.

[61] D. Gerosa, M. Kesden, R. O'Shaughnessy, A. Klein, E. Berti, U. Sperhake, and D. Trifirò, Physical Review Letters **115**, 141102 (2015), arXiv:1506.09116 [gr-qc].

[62] T. B. Littenberg, B. Farr, S. Coughlin, V. Kalogera, and D. E. Holz, ApJL **807**, L24 (2015), arXiv:1503.03179 [astro-ph.HE].

[63] R. N. Lang and S. A. Hughes, Phys. Rev. D **74**, 122001 (2006), gr-qc/0608062.

[64] R. N. Lang, S. A. Hughes, and N. J. Cornish, Phys. Rev. D **84**, 022002 (2011), arXiv:1101.3591 [gr-qc].

[65] B. Miller, R. O'Shaughnessy, T. B. Littenberg, and B. Farr, Phys. Rev. D **92**, 044056 (2015), arXiv:1506.06032 [gr-qc].

[66] S. Kullback and R. A. Leibler, Ann. Math. Statist. **22**, 79 (1951).

[67] U. von Toussaint, Reviews of Modern Physics **83**, 943 (2011).

[68] R. O'Shaughnessy, Phys. Rev. D **88**, 084061 (2013).

[69] C. P. L. Berry and J. R. Gair, MNRAS **435**, 3521 (2013), arXiv:1307.7276 [astro-ph.HE].

[70] S. Seehars, A. Amara, A. Refregier, A. Paranjape, and J. Akeret, Phys. Rev. D **90**, 023533 (2014), arXiv:1402.3593.

[71] H.-S. Cho and C.-H. Lee, Classical and Quantum Gravity **31**, 235009 (2014), arXiv:1403.4681 [gr-qc].

[72] I. Mandel, C. P. L. Berry, F. Ohme, S. Fairhurst, and W. M. Farr, Classical and Quantum Gravity **31**, 155005 (2014), arXiv:1404.2382 [gr-qc].